Mechatronics 54 (2018) 78–93

Contents lists available at ScienceDirect

Mechatronics

journal homepage: www.elsevier.com/locate/mechatronics

Disturbance observer based dynamic load torque compensator for assistive exoskeletons☆

Nauman Masud[a,b,*], Christian Smith[b], Magnus Isaksson[a]

[a] Department of Electronics Mathematics and Science, University of Gävle 80176, Sweden
[b] Department of Robotics, Perception and Learning, Royal Institute of Technology, Stockholm 100 44, Sweden

ARTICLE INFO

Keywords:
Load torque compensator
Exoskeleton
Serial manipulator
Disturbance observer

ABSTRACT

In assistive robotics applications, the human limb is attached intimately to the robotic exoskeleton. The coupled dynamics of the human-exoskeleton system are highly nonlinear and uncertain, and effectively appear as uncertain load-torques at the joint actuators of the exoskeleton. This uncertainty makes the application of standard computed torque techniques quite challenging. Furthermore, the need for safe human interaction severely limits the gear ratio of the actuators. With small gear ratios, the uncertain joint load-torques cannot be ignored and need to be effectively compensated. A novel disturbance observer based dynamic load-torque compensator is hereby proposed and analysed for the current controlled DC-drive actuators of the exoskeleton, to effectively compensate the said uncertain load-torques at the joint level. The feedforward dynamic load-torque compensator is proposed based on the higher order dynamic model of the current controlled DC-drive. The dynamic load-torque compensator based current controlled DC-drive is then combined with a tailored feedback disturbance observer to further improve the compensation performance in the presence of drive parametric uncertainty. The proposed compensator structure is shown both theoretically and practically to give significantly improved performance w.r.t disturbance observer compensator alone and classical static load-torque compensator, for rated load-torque frequencies up to 1.6 Hz, which is a typical joint frequency bound for normal daily activities for elderly. It is also shown theoretically that the proposed compensator achieves the improved performance with comparable reference current requirement for the current controlled DC-drive.

1. Introduction

Increase in elderly population in the society has driven active research in field of assistive exoskeletons so to enable the elderly to stay active and independently perform their daily activities [1,2]. Human-exoskeleton coupled dynamics is a key consideration in developing and realizing effective control methodologies for the needed body-worn devices. The human limb is mostly physically attached to an exoskeleton at the point of support. The nonlinear dynamics of the human is therefore coupled to the dynamics of exoskeleton at the point of interaction (contact) as pointed out by Hogan and Colgate [3,4]. The dynamics of human limbs are not only nonlinear but uncertain as well, as human tend to change their dynamics rapidly while performing their daily tasks [5–8]. Furthermore, the dynamics of the exoskeleton (which are essentially the dynamics of a serial manipulator) are also very nonlinear and generally have some associated uncertainty [9,10]. Therefore, this uncertainty in human dynamics coupled with uncertainty of the exoskeleton make the human-exoskeleton a highly nonlinear and uncertain system. It is shown in this paper that the uncertain dynamics of the human-exoskeleton system effectively appear as an uncertain load-torque at each joint of the exoskeleton actuators. DC-drives are generally selected as the joint actuators for the assistive exoskeletons for their high controllability, efficiency and range of motion [11–13]. High performance exoskeletons for effective assistance require actuators with high torque at considerably high speeds [14].This torque-speed requirement should be met with minimum possible weight, backlash and friction. Furthermore, to ensure human safety, the joints of the exoskeleton need to be back drivable with low reflected inertia [15,16]. All these requirements in turn require the gear ratio of the joint actuators to be small. Therefore, for exoskeletons with small gear ratios, the effect of load-torques containing the uncertain human dynamics on the actuator motors cannot be ignored. The standard computed torque control techniques for robotic manipulators [17–19], which inherently rely on an accurate inverse-dynamic model

☆ This paper was recommended for publication by Associate Editor Zhiyong Chen.

* Corresponding author.
E-mail address: Nauman.Masud@hig.se (N. Masud).

https://doi.org/10.1016/j.mechatronics.2018.07.003
Received 7 September 2017; Received in revised form 11 July 2018; Accepted 17 July 2018

of the system, can therefore not be used for task space control of lower gear ratio exoskeleton systems.

The task-space position control of the exoskeleton system can also be achieved by using classical independent-joint-control techniques [9,16], where task space position requirements can be translated into n joint level desired position trajectories, which can then be tracked independently by using the joint-space controllers. To compensate for the load-torque disturbance in this case, each joint controller should then exhibit good tracking performance which in turn requires high loop gain of the joint level system [20]. High loop gain lowers the joint level sensitivity, which in turn improve the disturbance rejection performance. Joint controllers with high gains are hence required to ensure sufficient closed-loop-bandwidth and hence low sensitivity for the joint level system [21]. This in turn can severely affect the quality of the system response as saturation based nonlinearities can be introduced into the system [22–24]. Thus, the limit on the gain of the joint-servo system, and hence on the gain of the joint controller, limits the ability of the controller to cancel the load-torque disturbances for the respective actuator. For sensor-less load-torque compensation, different torque estimators have also been proposed in literature for the DC-drive actuators [25–29]. Torque estimators based on robust techniques for DC-drives have been discussed in [26,27] while adaptive torque estimators have been presented in [28,29].

In our opinion, while considering both the performance and design simplicity, an effective solution in this regard is to sense the load-torque at each joint and then to compensate it explicitly through a joint load-torque compensator. Several sensor based compensation techniques for DC-drives have also been proposed in the literature. Feed forward torque compensators are usually designed considering only the first order dynamics of the actuator, which results in an over simplified compensator as a static constant. A disturbance observer (DOB) based feedback compensator was originally proposed by Ohnishi [30]. Due to its design simplicity and performance, DOB has found good many applications in servo motion control [31–34]. The application of DOB for the robotic manipulators and exoskeletons has also appeared in the literature [35–37].

In contrast to the existing techniques of using only the feedback or feedforward compensators alone, a novel load-torque compensator structure for joint level actuator is proposed in this paper, by combining an accurately designed feedforward compensator with an appropriate DOB structure in feedback. The feedforward compensator is designed by considering the high order dynamics of the actuator, while the DOB-based-feedback structure is suggested to ensure superior performance of the compensated system even in the presence of actuator parametric uncertainty. If all the joint actuators of the exoskeleton are properly compensated, it is shown here that this would effectively linearize and decouple the joint space of the human-exoskeleton system. The linearized joint space thus would contain only the well-known linear dynamics of joint actuators. This in turn could then allow for independent linear joint space controllers to be designed for desired stability and robustness for the human-exoskeleton system.

In this paper, the design and analysis of a new joint level load-torque compensator for human-exoskeleton system is presented. Significance for this work is presented in Section 2. A detailed modelling of a current controlled DC (CCDC) drive is presented in Section 3. In Section 4 a new feedforward load-torque compensator is proposed that considers all the dynamics of the CCDC-drive and is referred here as the Dynamic Load-Torque Compensator (DLTC). It is shown here that when the CCDC-drive is modelled using the first order dynamics, DLTC simplifies to a classical static torque constant, referred here as the Static Load-Torque Compensator (SLTC). The performance of both the compensators is first compared under no modelling uncertainty and it is shown by simulation that the DLTC under this assumption significantly outperforms the classical SLTC. For a perturbed DC-Drive model, because of the uncertainty in the drive parameters, the ability of the DLTC to effectively cancel out the load-torque disturbance in the low frequency range is reduced. To further improve the DLTC performance in rejecting the load-torque under modelling uncertainties, a novel load-torque compensation structure is then proposed in Section 5. It uses the proposed DLTC compensator in feedforward and a tailored DOB in feedback for the DLTC compensated CCDC-drive. The analysis of joint level position control of the CCDC-drive with the proposed DOB-based-DLTC is presented in Section 6. The performance of the proposed compensators for a servo controlled CCDC-drive is simulated and compared in Section 7 using real parameters of CCDC-drive. Since a typical human joint frequency bound for normal daily activities of elderly (walking, sit to stand, picking and placing an object) is 1.6Hz [38,39], performance is compared theoretically under a rated load-torque disturbance of 2.5 Nm at a higher frequency of 5 Hz (see Section 7.2) with 10% parametric uncertainty in CCDC-drive parameters. It is shown that even under rated load-torque disturbance, the proposed DOB-based-DLTC gives a significantly improved performance as compared to the classical SLTC and DOB when used alone. The performance of the proposed compensator is also compared theoretically for armature-current reference-signal requirements. The improvement offered by the proposed compensator is experimentally verified in Section 8 using an x-PC-Target™ based experimental setup. The proposed compensator structure is practically shown to give more than 5-dB mean improvement w.r.t DOB-alone and a 12-dB mean improvement w.r.t SLTC-alone in rejecting the load-torque disturbance up to 1.6 Hz.

2. Significance for human exoskeleton system

To lay the basis for the design of a novel load-torque compensator, a 4-degree of freedom (DOF) human-exoskeleton system is shown in Fig. 1. If n is the DOF of the exoskeleton and $j = 1...n$ represent the j_{th} joint. Then q, $\dot{\boldsymbol{q}}$ and $\ddot{\boldsymbol{q}} \in \mathbb{R}^n$ respectively define the joint-space position, velocity and acceleration vectors of the exoskeleton. Whereas the components $q_j = \theta_{oj}$, $\dot{q}_j = w_{oj} = \dot{\theta}_{oj}$ and $\ddot{q}_j = \dot{w}_{oj} = \ddot{\theta}_{oj}$ respectively represent the angular position, velocity and acceleration of the j^{th} joint. If the exoskeleton is modeled as an n-DOF serial manipulator, then its rigid body dynamics are given by the Euler-Langrage model [8]. The torque requirement for the exoskeleton as a vector $\boldsymbol{\tau_{exo}} \in \mathbb{R}^n$ is therefore given by the coupled nonlinear dynamic equation as

$$\boldsymbol{M}_{exo}(\boldsymbol{q})\ddot{\boldsymbol{q}} + \boldsymbol{C}_{exo}(\boldsymbol{q}, \dot{\boldsymbol{q}})\dot{\boldsymbol{q}} + \boldsymbol{g}_{exo}(\boldsymbol{q}) = \tau_{exo}. \quad (1)$$

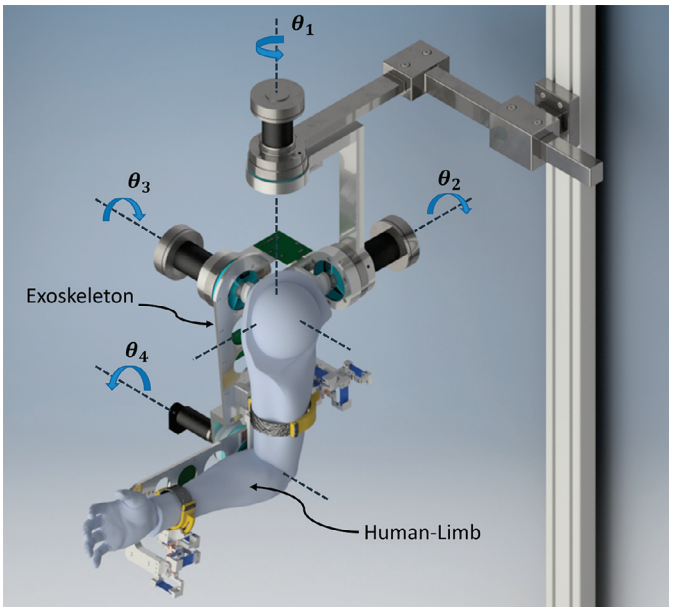

Fig. 1. 4-DOF Upper body exoskeleton with human-limb.

Table 1
Independent parameters for CCDC-drive.

Symbol	Quantity	Nominal values
R_a, R_{an}	Armature resistance	0.583 Ω
L_a, L_{an}	Armature inductance	1.191×10^{-4} H
k_s, k_{sn}	Motor Speed constant	$30.89\left(\frac{rad}{s}\right)V^{-1}$
$i_{a\max}$, $i_{a\max n}$	Maximum continuous current	3.62 A
J_m, J_{mn}	Motor rotor inertia	1.75×10^{-4} Kgm^2
w_{max}, w_{maxn}	Maximum rotor velocity	733 rad/s
i_0, i_{0n}	Motor No-load current	204×10^{-3} A
k_t, k_{tn}	Motor Torque constant	29.20×10^{-3} NmA^{-1}
J_g, J_{gn}	Gear moment of inertia	7×10^{-6} Kgm^2
F_g, F_{gn}	Gear viscous friction coefficient	1×10^{-3} $Nm\left(\frac{rad}{s}\right)^{-1}$
η	Gear ratio	25
p_{max}	Maximum percentage perturbation in actual parameters from the nominal	10%
t_s	Sampling time	10 μs
τ_{LR}	Rated load-torque at the motor	0.1 Nm

Where $\boldsymbol{M}_{exo}(\boldsymbol{q}) \in \mathbb{R}^{nxn}$ is the mass matrix, $\boldsymbol{C}_{exo}(\boldsymbol{q}, \dot{\boldsymbol{q}}) \in \mathbb{R}^{nxn}$ is the Coriolis's matrix and $\boldsymbol{g}_{exo}(\boldsymbol{q}) \in \mathbb{R}^n$ is the gravity vector of the exoskeleton. If the exoskeleton is assumed to be sufficiently rigid (i.e. it allows motions only along its DOF axes) then the DOF of supported human-limb is also effectively n. In addition, if DOF axes of human-limb are assumed to be perfectly aligned with those of the exoskeleton then $\boldsymbol{q}$,$\dot{\boldsymbol{q}}$ and $\ddot{\boldsymbol{q}}$ vectors would be the same for human-limb as well. If no voluntary human interaction is assumed, then the passive human-limb can be modelled in terms of its inertial terms by using the rigid body dynamics [6]. But if voluntary human interaction is considered then considering only inertial terms of the limb is not sufficient. This is because humans tend to not only apply a voluntary torque at each of their joints but can also introduce variable damping and stiffness in the limb by using their antagonist and agonist muscles [40]. Therefore, modelling human-limb with voluntary interaction needs additional terms for voluntary human torque, damping and stiffness [41,42]. The human-limb torque requirement $\boldsymbol{\tau_h} \in \mathbb{R}^n$ is therefore given by the nonlinear dynamic equation as

$$\boldsymbol{M}_h(\boldsymbol{q})\ddot{\boldsymbol{q}} + (\boldsymbol{C}_h(\boldsymbol{q}, \dot{\boldsymbol{q}}) + \boldsymbol{B_{hv}})\dot{\boldsymbol{q}} + \boldsymbol{g}_h(\boldsymbol{q}) + \boldsymbol{K}_{hv}(\boldsymbol{q} - \boldsymbol{q_o}) - \tau_{hv} = \tau_h. \quad (2)$$

Where $\boldsymbol{M}_h(\boldsymbol{q}) \in \mathbb{R}^{nxn}$ is the human mass matrix, $\boldsymbol{C}_h(\boldsymbol{q}, \dot{\boldsymbol{q}}) \in \mathbb{R}^{nxn}$ is the human Coriolis's matrix and $\boldsymbol{g}_h(\boldsymbol{q}) \in \mathbb{R}^n$ is the gravity vector of the of the human limb. $\boldsymbol{B_{hv}}$ and $\boldsymbol{K_{hv}} \in \mathbb{R}^{nxn}$ represents the diagonal voluntary damping and stiffness matrix of the human where $\boldsymbol{q_o} \in \mathbb{R}^n$ is the most recent joint position at which any component of $\boldsymbol{K_{hv}}$ becomes greater that zero. is the net voluntary torque exerted by the human. The uncertain variation in τ_{hv}, $\boldsymbol{B_{hv}}$ and $\boldsymbol{K_{hv}}$ by the humans therefore introduce a significant amount of uncertainty in estimation of $\boldsymbol{\tau_h}$ [41]. For complete assistance of the human limb by the exoskeleton, the net torque requirement $\boldsymbol{\tau_{Lo}} \in \mathbb{R}^n$ is given from (1) and (2) by a net nonlinear dynamic equation as

$$\boldsymbol{M}_{net}(\boldsymbol{q})\ddot{\boldsymbol{q}} + \boldsymbol{C}_{net}(\boldsymbol{q}, \dot{\boldsymbol{q}})\dot{\boldsymbol{q}} + \boldsymbol{g}_{net}(\boldsymbol{q}) + \boldsymbol{K_{hv}}(\boldsymbol{q} - \boldsymbol{q_o}) - \tau_{hv} = \tau_{exo} + \tau_h = \tau_{Lo}, \quad (3)$$

where

$$\boldsymbol{M}_{net}(\boldsymbol{q}) = \boldsymbol{M}_{exo}(\boldsymbol{q}) + \boldsymbol{M}_h(\boldsymbol{q}),$$
$$\boldsymbol{C}_{net}(\boldsymbol{q}, \dot{\boldsymbol{q}}) = \boldsymbol{C}_{exo}(\boldsymbol{q}, \dot{\boldsymbol{q}}) + \boldsymbol{C}_h(\boldsymbol{q}, \dot{\boldsymbol{q}}) + \boldsymbol{B_{hv}},$$
$$\boldsymbol{g}_{net}(\boldsymbol{q}) = \boldsymbol{g}_{exo}(\boldsymbol{q}) + \boldsymbol{g}_h(\boldsymbol{q}).$$

Any uncertainty in exoskeleton kinematics and the flexibility of its joints and links, results in uncertain estimation of the torque requirement for the exoskeleton $\boldsymbol{\tau_{exo}}$ in (1), which in turn adds to the uncertainty of $\boldsymbol{\tau_{Lo}}$ in (3). Furthermore, any misalignment between human and exoskeleton axes of rotation (which would always be there) would result in additional uncertain human torques, which would further increase the uncertainty in $\boldsymbol{\tau_{Lo}}$.

Table 2
Dependent parameters for CCDC-drive.

Symbol	Quantity	Relationship	Nominal values
k_a, k_{an}	Electrical gain	$\frac{1}{R_a}$, $\frac{1}{R_{an}}$	1.7153 Ω^{-1}
τ_a, τ_{an}	Electrical time constant	$\frac{L_a}{R_a}$, $\frac{L_{an}}{R_{an}}$	3.27×10^{-4} s
k_b, k_{bn}	Back EMF constant	$\frac{1}{k_s}$, $\frac{1}{k_{sn}}$	32.4 x 10^{-3} $V\left(\frac{rad}{s}\right)^{-1}$
T_f, T_{fn}	Motor viscous friction torque	$(i_0.k_t)$, $(i_{0n}.k_{tn})$	60×10^{-4} Nm
F_m, F_{mn}	Motor viscous friction coefficient	$\frac{T_f}{w_{max}}$, $\frac{T_{fn}}{w_{maxn}}$	8.13×10^{-6} $Nm\left(\frac{rad}{s}\right)^{-1}$
K_m, K_{mn}	Motor mechanical gain	$\frac{1}{F_m}$, $\frac{1}{F_{mn}}$	1.23×10^5 $\frac{rad}{s}(Nm)^{-1}$
τ_m, τ_{mn}	Motor mechanical time constant	$(K_m.J_m)$, $(K_{mn}.J_{mn})$	21.53 s
F_n, F_{nn}	Net viscous friction coefficient	$\left(F_m + \frac{F_g}{(\eta)^2}\right)$, $\left(F_{mn} + \frac{F_{gn}}{(\eta)^2}\right)$	9.72×10^{-6} $Nm\left(\frac{rad}{s.}\right)^{-1}$
J_n, J_{nn}	Net moment of inertia	$\left(J_m + \frac{J_g}{(\eta)^2}\right)$, $\left(J_{mn} + \frac{J_{gn}}{(\eta)^2}\right)$	1.75×10^{-4} Kgm^2
K_n, K_{nn}	Net mechanical gain	$\frac{1}{F_n}$, $\frac{1}{F_{nn}}$	1.02×10^5 $\frac{rad}{s}(Nm)^{-1}$
τ_n, τ_{nn}	Net mechanical time constant	$(K_n.J_n)$, $(K_{nn}.J_{nn})$	18 s

It is therefore clear from (3) that the dynamics of human-exoskeleton system is highly nonlinear, coupled and uncertain. Therefore, the standard computed torque control strategies for serial robotic manipulators [17–19] which strongly rely on accurate inverse-dynamic model of the system cannot directly be used. All the uncertain nonlinear dynamics of both the exoskeleton and the human are therefore contained in the net load-torque vector $\boldsymbol{\tau_{Lo}}$ and hence in its components $[\tau_{Lo1}, ...\tau_{Lo\,j}, ...\tau_{Lon}]$. It is worth noting that $\boldsymbol{\tau_h}$ cannot explicitly be measured by sensing the joint load-torques. This uncertainty and nonlinearity in $\boldsymbol{\tau_{Lo}}$ is hence linked to the exoskeleton, as $\boldsymbol{\tau_{Lo}}$ has to invariably be provided by the n joint actuators of the exoskeleton.

For the joint-actuator as a CCDC-drive, the approximate dynamic model is derived in the appendix and is given by (A.18). The parameters of the drive are defined in Tables 1–3. The model for the j^{th} actuator in time domain is therefore written in terms of $\dot{q}_j$ and $\ddot{q}_j$ as

$$\left(\eta^2\frac{\tau_A}{K_A}\right)_j\ddot{q}_j + \left(\frac{\eta^2}{K_A}\right)_j\dot{q}_j = (\eta i^*_{as})_j - f_{nj}, \quad (4)$$

where $f_{n\,j} = \left(\frac{K_B}{\eta K_A}\right)_j \tau_{Lo\,j}$.

f_{nj} in (4) represents the load-torque dependent nonlinearity of the j^{th} joint. It is therefore noted that the uncertain nonlinear dynamics of the human-exoskeleton system are linked to the j^{th} joint actuator through its respective load-torque τ_{Loj}. This in turn makes the linear model of the

Table 3
Parameters for PWM converter for CCDC-drive.

Symbol	Quantity	Nominal values
f_c	Converter switching frequency	56.3×10^3 Hz
t_r	Converter sample time = $\frac{1}{f_c}$	1.776×10^{-5} s
V_{dc}	Converter input DC voltage	24 V
v_{cmax}	Maximum control voltage	10 V
K_r, K_{rn}	Converter gain	2.4
I_{amax}	Maximum armature current	15 A
I_{smax}	Maximum sensed current	10 V
H_c	Current feedback Gain	0.667 VA^{-1}
K_c	Current Controller Gain	800

joint actuator to become coupled, nonlinear and uncertain. Therefore, the overall joint level nonlinear dynamics for an n-DOF human-exoskeleton system with actuator dynamics follows from (4) as

$$\boldsymbol{H}^2\boldsymbol{M}_D\ddot{\boldsymbol{q}} + \boldsymbol{H}^2\boldsymbol{B}_D\dot{\boldsymbol{q}} = \boldsymbol{H}\boldsymbol{i}^*_{as} - \boldsymbol{f}_n, \tag{5}$$

where

$$\boldsymbol{H} = diag\{\eta_j\} \in \mathbb{R}^{nxn},$$

$$\boldsymbol{M}_D = diag\left\{\left(\frac{\tau_A}{K_A}\right)_j\right\} \in \mathbb{R}^{nxn},$$

$$\boldsymbol{B}_D = diag\left\{\left(\frac{1}{K_A}\right)_j\right\} \in \mathbb{R}^{nxn},$$

$$\boldsymbol{i}^*_{as} = vec(i^*_{as\,j}) \in \mathbb{R}^n,$$

$$\boldsymbol{f}_n = vec(f_{n\,j}) \in \mathbb{R}^n.$$

$\boldsymbol{f}_n$ in (5) represents the net uncertainty and nonlinearity in the overall system. The effect of this term can be minimized by making the matrix $\boldsymbol{H}$ large i.e. by increasing the gear ratio of all the n actuators. Increase in $\boldsymbol{H}$ apart from increasing the weight and size of the actuators increases both the apparent mass matrix $\boldsymbol{M}_D$ and damping matrix $\boldsymbol{B}_D$ of the actuators by $\boldsymbol{H}^2$. Therefore, a decrease in nonlinearity is achieved at the expense of increase in weight, size and apparent impedance of the exoskeleton. An increased apparent impedance of the exoskeleton can cause large human-exoskeleton interactive forces which can make the overall system unsafe for close human interaction [3,4]. Furthermore, as seen from the frequency domain model of the actuator in (A.18), an increased η reduces the gain and hence the output-bandwidth of the actuator. This in turn reduces the bandwidth and speed of response of the overall system.

As a better alternative, it is proposed to explicitly sense the joint load-torque τ_{Loj} and then use advanced compensation techniques to effectively linearize the dynamics of the j^{th} actuator. Therefore, with effective torque compensation applied, the model for the j^{th} joint actuator can be written as

$$\left(\eta^2\frac{\tau_A}{K_A}\right)_j\ddot{q}_j + \left(\frac{\eta^2}{K_A}\right)_j\dot{q}_j = (\eta i^*_{as})_j + \left(f_j - f_{nj}\right) = (\eta i^*_{as})_j + e_{ucj}. \tag{6}$$

Where f_j is the compensation applied and e_{ucj} is the error in compensation of the j^{th} load-torque and represents the associated uncompensated uncertain nonlinearity. If all the n actuators are effectively compensated, then, by using the approximate model of the actuator, the overall dynamics of a compensated n-DOF human-exoskeleton system is given from (6) as

$$\boldsymbol{H}^2\boldsymbol{M}_D\ddot{\boldsymbol{q}} + \boldsymbol{H}^2\boldsymbol{B}_D\dot{\boldsymbol{q}} = \boldsymbol{H}\boldsymbol{i}^*_{as} + \boldsymbol{e}_{uc}, \tag{7}$$

where $\boldsymbol{e}_{uc} = vec\left(f_j - f_{nj}\right) = vec(e_{ucj}) \in \mathbb{R}^n$.

It is noted from (7), that provided the uncompensated-uncertain-nonlinearity vector $\boldsymbol{e}_{uc}$ is sufficiently small in magnitude as compared to the vector $\boldsymbol{H}\boldsymbol{i}^*_{as}$, the overall dynamics of the human-exoskeleton system is effectively linear and certain. Therefore, to keep $\boldsymbol{e}_{uc}$ small, advanced compensation techniques need to be used. This requirement hence sets the basis to develop and evaluate effective joint-level compensation techniques for decoupling and linearization of overall human-exoskeleton system with small or unity gear ratios. For the development and evaluation of load-torque compensation strategies a single joint with CCDC-drive as an actuator is considered. The j subscript is therefore dropped for notation simplicity.

3. Modelling of current controlled DC-drive

The actuators play a key role in the control of any robotic serial manipulator as the task space accuracy of the manipulator is mainly dependent on the joint actuators accuracy and their resolution of control [9]. The accuracy of the actuator control in turn is primarily dependent on its ability to reject the unwanted load-torque disturbances. The ability of the CCDC-drives to reliably and efficiently generate and control the desired torque makes them the best actuator to use for serial manipulators, as the desired torque can be explicitly modulated to reject the load-torque disturbances. Generally, in the literature, first order models of the CCDC-drive have been considered [43,44] with little attention paid to higher order models. To design an accurate feedforward compensator, an accurate model of the CCDC-drive is required. A four-quadrant CCDC-drive mainly consists of a four-quadrant power converter, a geared DC motor and a current controller to control the motor's desired armature current in feedback [45]. A block diagram of the CCDC-drive is shown in Fig. 2. The dynamics of all three components have been considered to accurately model the drive. The nominal and actual parameters for the drive are defined and listed in Tables 1–3. The detailed modelling of the CCDC-drive by using the defined parameters is presented in Appendix A.

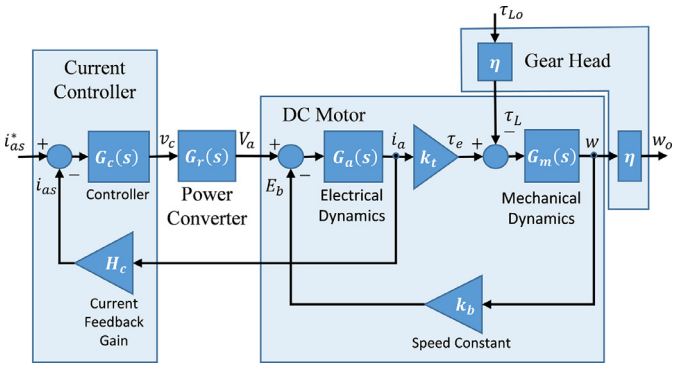

Fig. 2. Block diagram CCDC-drive.

If i^*_{as} is the armature current reference in volts, τ_{Lo} is the load-torque at the output shaft and w_o is the output angular velocity then an accurate frequency domain model of the CCDC-drive is derived in terms of its inputs i^*_{as} and τ_{Lo} and is given from (A.10) as

$$w_o = \frac{1}{\eta}\,G_A(s)\,i^*_{as} - \frac{1}{\eta^2}G_B(s)\,\tau_{Lo}, \tag{8}$$

where
$$G_A(s) = \frac{G_c(s)G_r(s)G_{zoh}(s)}{D_f(s)},$$
$$G_B(s) = G_D(s) + G_2(s),$$
$$G_D(s) = \frac{H_cG_c(s)\,G_t(s)G_r(s)}{D_f(s)},$$
$$D_f(s) = (1 + H_cG_c(s)G_r(s)G_a(s))\,.$$

To evaluate the performance of the proposed compensator for the CCDC-drive, in the presence of drive parametric uncertainty, a nominal model of CCDC-drive in terms of the nominal drive parameters is given from (8) as

$$w_o = \frac{1}{\eta}G_{A_n}(s)\,i^*_{as} - \frac{1}{\eta^2}G_{B_n}(s)\,\tau_{Lo}\,. \tag{9}$$

Where $G_{A_n}(s)$ and $G_{B_n}(s)$ define the nominal dynamics from i^*_{as} to w_o and τ_{Lo} to w_o respectively, using the nominal drive parameters. All the transfer functions defining $G_A(s)$, $G_{A_n}(s)$, $G_B(s)$ and $G_{B_n}(s)$ are defined in Appendix A.

4. Feed-forward load-torque compensators

4.1. Dynamic load-torque compensator

A concept of a new feedforward dynamic load-torque compensator (DLTC), using the derived higher order model of the CCDC-drive in (8), is shown in Fig. 3. The concept is to sense the joint load-torque τ_{Lo} on the drive and then to modulate the desired current i^*_{as}, to not only compensate the effect of τ_{Lo} on w_o but also to ensure that the i^*_{as} based

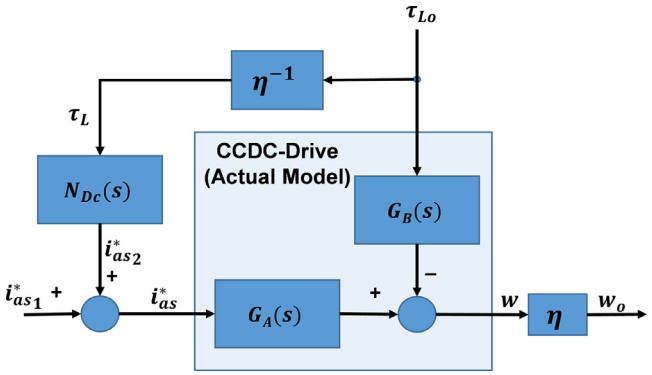

Fig. 3. Proposed DLTC scheme for the CCDC-drive.

velocity control of the drive is not effected in anyway. It is hence proposed to decompose i^*_{as} as

$$i^*_{as} = i^*_{as1} + i^*_{as2}\,. \tag{10}$$

Where i^*_{as1} represents the part of the desired current to be modulated, to control the drive's velocity (which can be generated by a separate position or velocity controller) while i^*_{as2} is the part of desired current to be modulated, to cancel the effect of load-torque disturbance. It is suggested that i^*_{as2} can be designed to be given in terms of the dynamic load-torque compensator $N_{Dc}(s)$, defined as

$$N_{Dc}(s) = \frac{i^*_{as2}}{\tau_L} = \frac{G_{B_n}(s)}{G_{A_n}(s)},\ \ i^*_{as2} = N_{Dc}(s)\,\tau_L\,. \tag{11}$$

Where τ_L is the load-torque at the motor shaft and is given by $\tau_L = \frac{\tau_{Lo}}{\eta}$. The actual dynamic of the CCDC-drive-in terms of i^*_{as1} and τ_{Lo} can be written from (8), (10) and (11) as

$$w_o = \frac{1}{\eta}G_A(s)i^*_{as1} + \frac{1}{\eta^2}\left(G_A(s)\frac{G_{B_n}(s)}{G_{A_n}(s)} - G_B(s)\right)\tau_{Lo}. \tag{12}$$

It is evident from (12) that the ability of the DLTC in cancelling the load-torque disturbance depends on how well the drive dynamics have been modelled, i.e. how close the nominal transfer functions $G_{A_n}(s)$ and $G_{B_n}(s)$ are to their actual counterparts $G_A(s)$ and $G_B(s)$ respectively, over whole of the drive bandwidth. Under ideal modelling assumptions, i.e. for $G_{A_n}(s) \approx G_A(s)$ and $G_{B_n}(s) \approx G_B(s)$ we have form (12)

$$w_o \approx \frac{1}{\eta}G_A(s)\,i^*_{as1}, \tag{13}$$

i.e. the gain for τ_{Lo} input has been completely compensated by the DLTC and the drive velocity is completely independent of the load of the torque disturbance. To facilitate the implementation of the DLTC an explicit expression for $N_{Dc}(s)$ is found in terms of nominal motor parameters from (A.1) to (A.15) and is given as

$$N_{Dc}(s) = (t_s\tau_{a_n}t_r s^4 + (2t_s\tau_{a_n} + t_s t_r + 2\tau_{a_n}t_r)s^3 + (2t_s + 4\tau_{a_n} + 2t_r)s^2 + (2t_s H_c K_c K_{r_n} k_{a_n} + 4)s + 4H_c K_c K_{r_n} k_{a_n})/(K_c K_{r_n} k_{a_n} k_{t_n}). \tag{14}$$

It is evident from (14) that $N_{Dc}(s)$ is improper hence needs a series low pass filter of order greater than or equal to four for its implementation. A sixth-order low pass filter $Q_{Dc}(s)$, having the form shown in (15) is suggested. This filter is characterized for its simplicity, small phase distortion, sufficient roll-off and near unity gain over its bandwidth. The filter $Q_{Dc}(s)$ is hence given as

$$Q_{Dc}(s) = \frac{\left(\frac{1}{0.98\omega_c}s + 1\right)}{\left(\frac{1}{\omega_c}s + 1\right)^6}\,. \tag{15}$$

To select a proper cut-off frequency ω_c for the filter $Q_{Dc}(s)$, it is important to know the location of the zeroes of $N_{Dc}(s)$. As seen from (14) the coefficients of the numerator-polynomial of $N_{Dc}(s)$, in addition to being a function of the drive parameters are also a function of the sampling time t_s. The zeros of $N_{Dc}(s)$ and hence their respective corner frequencies are found as a function of t_s for the nominal drive parameters listed in Tables 1–3. It is found that for the given drive parameters, $N_{Dc}(s)$ has two real zeros and one quadratic zero. Variation of the corner frequencies of these zeros with respect to t_s is shown in Fig. 4, with t_s being varied from 10 μs to 110 μs. It is seen that the corner frequencies of both the real zeros decrease with increase in t_s, while that of the quadratic zero remain constant at 2588 rad/s. The corner frequency of the quadratic zeroes being the lowest give the dominant dynamics of $N_{Dc}(s)$. If the dynamics of $N_{Dc}(s)$ are not to be altered by the filter $Q_{Dc}(s)$, its cutoff frequency ω_c should be greater than the corner frequencies of all the zeros of $N_{Dc}(s)$.

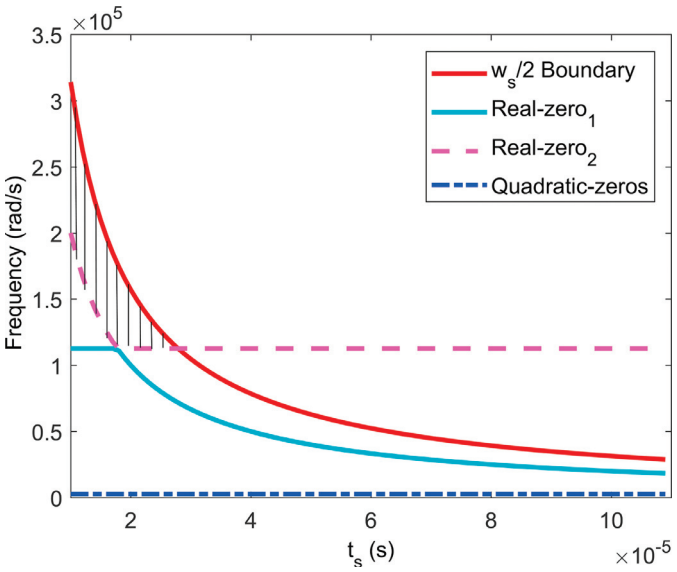

Fig. 4. The corner frequencies of $DLTC(N_{Dc}(s))$ are plotted as a function of t_s for the nominal CCDC-drive parameters listed in Tables 1–3 along with the suggested area for selection of the cut-off frequency ω_c for the filter $Q_{Dc}(s)$.

Also, if ω_s is the sampling frequency then $\omega_c \le \omega_s/2$ to satisfy the sampling requirement. For the chosen range of t_s (10 μs-110 μs) the region satisfying both the requirements for ω_c is shown shaded in Fig. 4. A cut-off frequency value of $\omega_c = \frac{\omega_s}{2} = 3.141 \times 10^5$ rad/s is chosen for the filter $Q_{Dc}(s)$ in (15). For this value of ω_c, the sampling time t_s is found from Fig. 4 to be 10 μs. A realizable DLTC as $N_{Dcf}(s)$ is hence defined from (14) and (15) as

$$N_{Dcf}(s) = \frac{i^*_{as2}}{\tau_L} = N_{Dc}(s)Q_{Dc}(s) = \frac{G_{B_n}(s)}{G_{A_n}(s)}Q_{Dc}(s). \tag{16}$$

With this definition of DLTC, (12) can then be written as

$$w_o = \frac{1}{\eta}G_A(s)i^*_{as1} + \frac{1}{\eta^2}\big(G_A(s)N_{Dcf}(s) - G_B(s)\big)\tau_{Lo}. \tag{17}$$

If $G_{uc}(s)_{dltc}$ is defined as

$$G_{uc}(s)_{dltc} = (G_A(s).\,N_{Dcf}(s) - G_B(s)), \tag{18}$$

then using (16), (18) can be written as

$$G_{uc}(s)_{dltc} = \left(G_A(s)\frac{G_{B_n}(s)}{G_{A_n}(s)}\,Q_{Dc}(s) - G_B(s)\right). \tag{19}$$

$|G_{uc}(s)_{dltc}|$ in (19) hence gives a measure of the frequency dependent uncompensated gain left by the DLTC due to modelling inaccuracy and therefore is a measure of the ability of the DLTC in cancelling the load-torque disturbance. Eq. (12) can therefore be written in terms of

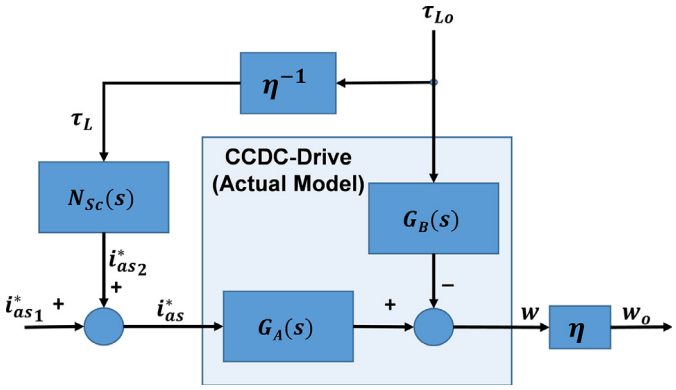

Fig. 5. Static load-torque compensator (SLTC) scheme for the CCDC-drive.

$G_{uc}(s)_{dltc}$ as

$$w_o = \frac{1}{\eta} G_A(s) i^*_{as1} + \frac{1}{\eta^2} G_{uc}(s)_{dltc} \tau_{Lo} \ . \tag{20}$$

By comparing (20) with (8) it is seen that DLTC reduces the frequency dependent load-torque disturbance gain from $G_B(s)$ to $G_{uc}(s)_{dltc}$. Ideal modelling ($G_{A_n}(s) \approx G_A(s)$, $G_{B_n}(s) \approx G_B(s)$) and filtering assumption $s(Q_{Dc}(s) \approx 1)$ imply from (19) that $G_{uc}(s)_{dltc} \approx 0$ over the bandwidth of $Q_{Dc}(s)$. Therefore, performance of the DLTC is perfect under these assumptions.

4.2. Static load-torque compensator

For the DC-drive system, whose actual dynamics are given by (8), a feedforward compensator can also be derived using the approximate model of CCDC-drive (given in Appendix A by (A.18)) on the same footing as that of DLTC. The concept is shown in Fig. 5. Therefore, $i^*_{as_2}$ for this case is similarly given by

$$i^*_{as_2} = \frac{G'_{B_n}(s)}{G'_{A_n}(s)} \tau_L \ . \tag{21}$$

With i^*_{as} given by (10), the dynamics of CCDC-drive-in terms of $i^*_{as_1}$ and τ_{Lo} can then be written from (8) (10) and (21) as

$$w_o = \frac{1}{\eta} G_A(s) i^*_{as1} + \frac{1}{\eta^2} \left(G_A(s) \frac{G'_{B_n}(s)}{G'_{A_n}(s)} - G_B(s) \right) \tau_{Lo}. \tag{22}$$

The feedforward compensator $N_{Sc}(s)$ for this case is referred as the static load-torque compensator (SLTC) and is defined from (21) as

$$N_{Sc}(s) = \frac{i^*_{as_2}}{\tau_L} = \frac{G'_{B_n}(s)}{G'_{A_n}(s)} = \frac{H_c}{k_{t_n}} \ . \tag{23}$$

It is hence seen from (23) that when the CCDC-drive is modelled as a first order system by ignoring the higher order dynamics, the feedforward compensator comes out to be a static constant. Frequency response of the unfiltered-DLTC, filtered-DLTC and SLTC are respectively shown in Fig. 6 for the nominal drive parameters. It is seen from Fig. 6 that the frequency response of filtered-DLTC and that of the unfiltered-DLTC are very similar within the bandwidth of filter $Q_{Dc}(s)$.

Therefore, the filter $Q_{Dc}(s)$ enables the DLTC to be realized without altering its key dynamics. It is also seen that though the DC-gains of DLTC and SLTC are the same, the frequency response of DLTC and SLTC are very different, signifying that SLTC is missing some key dynamics necessary for effective compensation of load-torque disturbance. The frequency dependent uncompensated gain left by SLTC is hence similarly given by

$$G_{uc}(s)_{sltc} = (G_A(s)\, N_{Sc}(s) - G_B(s)) \ . \tag{24}$$

The output-velocity w_o given by (22) is then written in terms of $G_{uc}(s)_{sltc}$ as

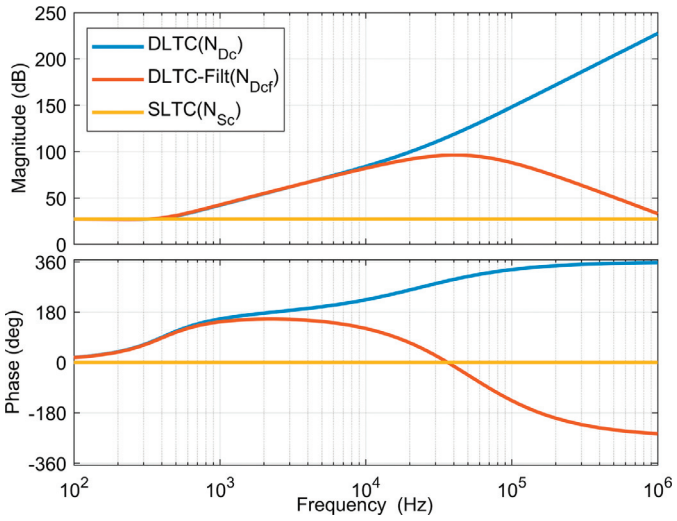

Fig. 6. Magnitude and phase response of unfiltered-DLTC ($N_{Dc}(s)$), filtered-DLTC ($N_{Dcf}(s)$) and SLTC ($N_{Sc}(s)$).

$$w_o = \frac{1}{\eta} G_A(s)\ i^*_{as1} + \frac{1}{\eta^2} G_{uc}(s)_{sltc}\ \tau_{Lo}. \tag{25}$$

4.3. Un-compensated gain comparison for DLTC and SLTC

In order to validate and compare the effectiveness of DLTC and SLTC in compensating for the load-torque disturbance, the uncompensated frequency dependent gains $|G_{uc}(s)_{dltc}|$ given by (19) and $|G_{uc}(s)_{sltc}|$ given by (24) are plotted vs frequency for comparison in Fig. 7. The parameters of CCDC-drive used are listed in Tables 1–3. The higher the uncompensated gain magnitude is at a frequency, the higher the expected load-torque disturbance is for that frequency. It is seen from Fig. 7 that for the ideal modelling case i.e. when $G_A(s) \approx G_{A_n}(s)$ and $G_B(s) \approx G_{B_n}(s)$, the response of $|G_{uc}(s)_{dltc(nominal)}|$ is 30 dB less than that of $|G_{uc}(s)_{sltc(nominal)}|$ over the whole of the bandwidth of the filter $Q_{Dc}(s)$. Therefore, for an accurate nominal model of the CCDC-drive, the DLTC is expected to have a superior performance in rejecting the load-torque disturbance as compared to SLTC. In practice though it is not always possible to exactly model the plant. The uncertainty in the drive parameters can effectively be considered as an additive uncertainty

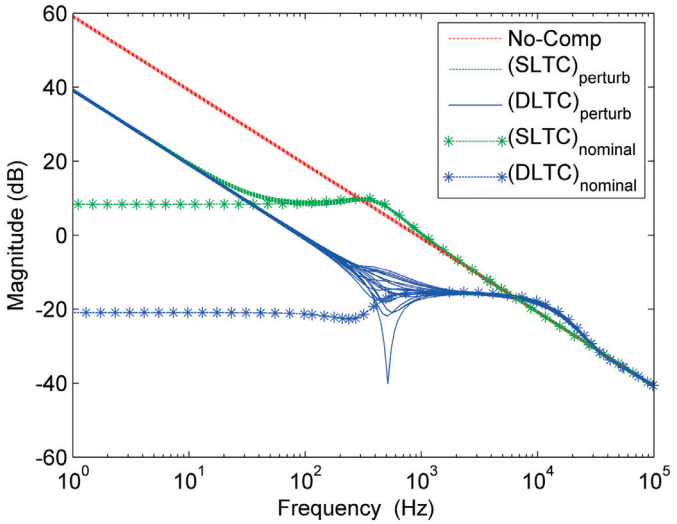

Fig. 7. Magnitude plots of $G_{uc}(s)_{sltc}$ and $G_{uc}(s)_{dltc}$ for nominal and perturbed cases for the drive parameters listed in Tables 1–3, along with the case when no compensator is used.

[20]. If the actual parameters of the drive are additively perturbed at the most by a fixed percentage p_{max}, then to compare the performance of DLTC and SLTC under a worst-case scenario, it is important to first identify the actual drive parameters that have a dominant effect on increasing the magnitude of uncompensated gains for both the compensators. As the DC-gain of $G_{uc}(s)_{dltc}$ or $G_{uc}(s)_{sltc}$ define the maximum possible magnitude, the parameters effecting the DC-gains are the dominant parameters effecting $G_{uc}(s)_{dltc}$ and $G_{uc}(s)_{sltc}$. The DC-gain of $G_{uc}(s)_{dltc}$ $G_{uc}(s)_{sltc}$ are derived from (19) and (24) respectively in terms of the drive's independent parameters (listed in Table 1) and are given as

$$|G_{uc}(s)_{dltc}|_{dc} = \left| \frac{w_{max}}{i_0 k_{tn}} - \frac{{w_{max}}^2 i_{0n}}{{i_0}^2 k_t w_{maxn}} \right|, \tag{26}$$

$$|G_{uc}(s)_{sltc}|_{dc} = \left| \frac{w_{max}}{i_0} \left(\frac{1}{k_{tn}} - \frac{1}{k_t} \right) \right| . \tag{27}$$

The actual parameters w_{max}, i_0, k_t are hence the dominant parameters, that have a dominant effect on both $|G_{uc}(s)_{dltc}|$ and $|G_{uc}(s)_{sltc}|$. If the dominant parameters are perturbed from the nominal as

$$\begin{aligned} w_{max} &= w_{max_n} + w_{max_n} \frac{p_{max}}{100}, \\ i_0 &= i_{0_n} - i_{0_n} \frac{p_{max}}{100}, \\ k_t &= k_{t_n} - k_{t_n} \frac{p_{max}}{100}, \end{aligned} \tag{28}$$

then both the DC-gains in (26) and (27) are a maximum. The plots of $|G_{uc}(s)_{dltc}|$ and $|G_{uc}(s)_{sltc}|$ are plotted in Fig. 7 for a worst case perturbed scenario, where the dominant actual drive parameters are given a fixed maximum perturbation as per (28). The rest of the actual drive parameters listed in Tables 1–3 are randomly perturbed form the nominal, at the most by p_{max}. It is seen that there is a small change in magnitude of both the plots with random variation of the non-dominant parameters. Hence plots of $|G_{uc}(s)_{dltc}|$ and $|G_{uc}(s)_{sltc}|$ under these perturbation conditions define the limit of uncompensated torque gains that can be expected at any frequency for the respective compensator. It is also seen from Fig. 7 that under these perturbed conditions, the performance of DLTC for low frequencies (< 16 Hz) deteriorates to that of SLTC. For frequencies greater than 16 Hz, DLTC outperform SLTC in rejecting the load toque disturbance. If no compensator is used then the uncompensated torque gain is maximum possible and is given by $|G_{uc}(s)_{max}| = |G_B(s)|$, which is also plotted in Fig. 7.

5. Disturbance observer based dynamic load-torque compensator

Even though DLTC is expected to give a good performance in compensating the load-torque in medium to high frequency range, its low frequency performance is seen to be effected by the drive's parametric uncertainties. To further improve the performance of DLTC in the presence of uncertainties, a novel compensator structure is suggested that uses the proposed DLTC as a feedforward compensator in conjunction with a feedback DOB for the DLTC compensated CCDC-drive. The concept is shown in Fig. 8.

5.1. Disturbance observer for DLTC compensated CCDC-drive

If τ_e^* is the electromegnatic torque to be generated, k_{tn} is the torque constant of the motor and H_c is the current feedback gain of the drive, then $i_{as_1}^*$ similar to $i_{as_2}^*$ can also be given from (23) as

$$i_{as_1}^* = \frac{H_c}{k_{t_n}} \tau_e^*. \tag{29}$$

If w is the motor-shaft velocity then $w_o = w/\eta$. Therefore for CCDC-drive with feedforward DLTC, w can then be written from (20) and (29) as

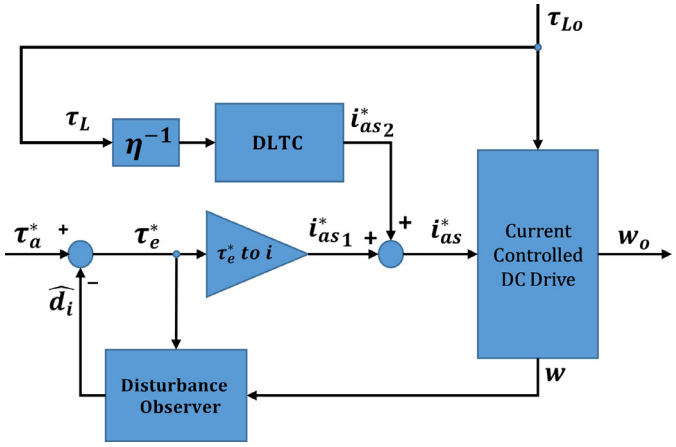

Fig. 8. An overview of the proposed DOB-based-DLTC structure for the CCDC-drive.

$$w = G_T(s)\, \tau_e^* + \frac{1}{\eta} G_{uc}(s)_{dltc}\, \tau_{Lo}, \tag{30}$$

where $G_T(s) = G_A(s) \frac{H_c}{k_{tn}}$.

If $G_{Tn}(s)$ represents the nominal forward torque dynamics then the actual forward torque dynamics $G_T(s)$ is represented as a multiplicative uncertainty model as [34] $G_T(s) = (1 + \Delta(s))\, G_{Tn}(s)$, for $\|\Delta\|_\infty \leq 1$. $G_T(s)$ can then be written in terms of disturbance dynamics as

$$G_T(s) = G_{T_n}(s) + D_T(s), \tag{31}$$

$$\begin{aligned} \text{where} \quad G_{T_n}(s) &= G'_{A_n}(s) \frac{H_c}{k_{t_n}}, \\ D_T(s) &= \Delta(s)\, G_{T_n}(s). \end{aligned}$$

$G'_{A_n}(s)$ in (31) is derived in Appendix A and is given by A.13). $D_T(s)$ in ((31) represents the part of the dynamics of $G_T(s)$ which is not included in the nominal $G_{Tn}(s)$. The motor-shaft velocity w can then be written in terms of $G_{Tn}(s)$ and disturbance d_o as

$$w = G_{Tn}(s).\, \tau_e^* + d_{1o} + d_{2o} = G_{Tn}(s) \tau_e^* + d_o . \tag{32}$$

Where d_o is the total output disturbance, $d_{1o} = D_T(s)\, \tau_e^*$ is the part of d_o due to mismatch between G_T and G_{Tn} and $d_{2o} = \frac{1}{\eta} G_{uc}(s)_{dltc} \tau_{Lo}$ represents the part of d_o due to uncompensated load-torque, left by DLTC. Since the output disturbance d_o should be compensated by manipulating the torque input τ_e^*, the corresponding input disturbance d_i is hence given from (32) in terms of d_o as

$$d_i = \frac{d_o}{G_T(s)} = \frac{w}{G_T(s)} - \frac{G_{Tn}(s)}{G_T(s)} \tau_e^* . \tag{33}$$

An estimate of the input disturbance $\widehat{d}_i$ in terms of the measured motor-shaft velocity w and the identified nominal dynamics $G_{Tn}(s)$ hence follows from (33) as

$$\widehat{d}_i = \frac{w}{G_{Tn}(s)} - \tau_e^*. \tag{34}$$

Since $G_{Tn}(s)$ is always proper, $1/\, G_{Tn}(s)$ is not realizable. A cascaded low pass filter $Q_o(s)$ is hence required for its proper implementation. A realizable disturbance observer that can give an estimate of the input disturbance $\widehat{d}_i$ follows from (34) as

$$\widehat{d}_i = G_o(s)\, w - Q_o(s)\, \tau_e^*, \tag{35}$$

where $G_o(s) = \frac{Q_o(s)}{G_{Tn}(s)}$.

If τ_a^* is the desired input acceleration torque, then the estimate of input disturbance $\widehat{d}_i$ must be subtracted from τ_a^* to obtain the electromagnetic torque τ_e^* to be generated by the drive as

$$\tau_e^* = \tau_a^* - \widehat{d}_i . \tag{36}$$

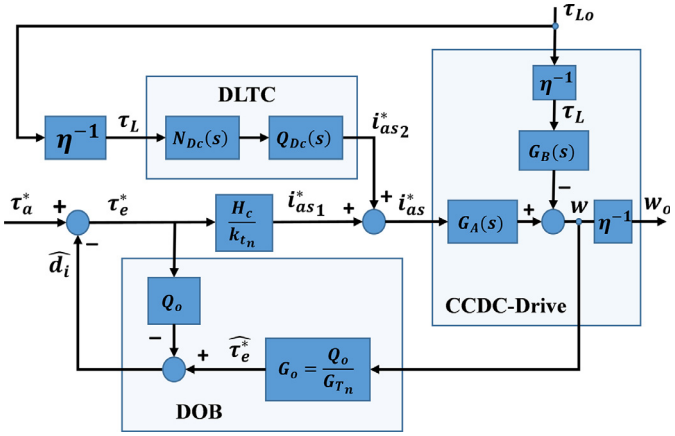

Fig. 9. Detailed structure of the proposed DOB-based-DLTC for the CCDC-drive.

This formulation of DOB along with DLTC for the CCDC- drive is given by (30) and (35) and is shown in detail in Fig. 9. For the closed-loop system in Fig. 9 to be internally stable with the DOB given by (35) in feedback, it is required that the magnitude of the filter $Q_o(s)$ is bounded as [31]

$$|Q_o(s)| \leq \left|\frac{1}{\Delta(s)}\right| . \tag{37}$$

Whereas for good tracking reponse of the system it is required that $|Q_o(s)| \approx 1$. Therefore the filter $Q_o(s)$ has to be carefully selected to ensure both stability and performance.

The filter $Q_o(s)$ is hence choosen to be of the form

$$Q_o(s) = 1.1\ \omega_{oc}{}^2 \frac{(s + 0.9\omega_{oc})}{(s + \omega_{oc})^3} . \tag{38}$$

The associated multiplicative uncertainity in $G_T(s)$ is given from (31) as

$$\frac{1}{\Delta(s)} = \frac{G_{Tn}(s)}{G_T(s) - G_{Tn}(s)} . \tag{39}$$

The corresponding plots of $\left|\frac{1}{\Delta(s)}\right|$ are shown in Fig. 10, for actual parameters of the drive being additively perturbed at random, at the most by p_{max}. For the stabililty condition in (37) to be satisfied for all $\left|\frac{1}{\Delta(s)}\right|$ curves, the cut-off frequency ω_{oc} for $Q_o(s)$ is chosen to be $0.2\omega_n$. Where ω_n is the bandwidth of the nominal forward system $G_{Tn}(s)$. For $Q_o(s)$ given by (38) and at chosen ω_{oc}, it is seen from Fig. 10 that the stability condition in (37) is satisfied for all $\left|\frac{1}{\Delta(s)}\right|$ curves. Therefore, the DOB based closed-loop system in Fig. 9 is expected to be internally stable. For nominal drive parameters listed in Tables 1–3, the bandwidth ω_n is found to be 5.7×10^3 rad/s(910Hz), which in turn gives $\omega_{oc} = 2.85 \times 10^3$ rad/s(453 Hz).

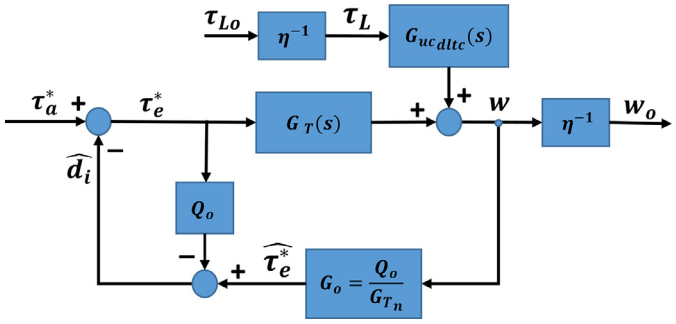

Fig. 11. Simplified structure for proposed DOB-based-DLTC for CCDC-drive in terms of $G_T(s)$ and $G_{uc}(s)_{dltc}$.

The motor-shaft velocity w of the drive, in terms of $G_T(s)$ and $G_{uc}(s)_{dltc}$ is given by (30). This in-turn is used to simplify the DOB-based-DLTC structure of Fig. 9. The simplified scheme is shown in Fig. 10. The referred electromagnetic torque τ_e^* in Fig. 11 is therefore given from (35) and (36) as

$$\tau_e^* = \frac{\tau_a^*}{1 - Q_o(s)} - \frac{Q_o(s)}{G_{Tn}(s)(1 - Q_o(s))} w . \tag{40}$$

Output angular velocity w_o of the complete closed-loop compensated system of Fig. 11, can then be written from (30) and (40), in terms of the inputs τ_a^* and τ_{Lo} as

$$w_o = \frac{1}{\eta} G_T(s)_{net}\ \tau_a^* + \frac{1}{\eta^2} G_{uc}(s)_{net}\ \tau_{Lo}, \tag{41}$$

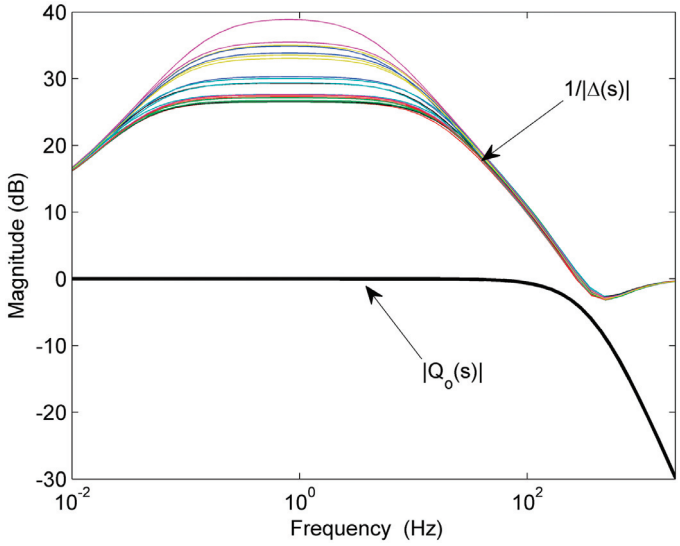

Fig. 10. Showing $|Q_o(s)|$ is always less than all $\left|\frac{1}{\Delta(s)}\right|$ curves for all frequencies. Where corresponding $\left|\frac{1}{\Delta(s)}\right|$ is plotted for actual parameters of the drive being additively perturbed at random at most by p_{max} percentage.

where $G_T(s)_{net} = \frac{G_T(s)\, G_{Tn}(s)}{D(s)_{net}}$,

$$G_{uc}(s)_{net} = \frac{G_{Tn}(s)(1 - Q_o(s))G_{uc}(s)_{dltc}}{D(s)_{net}},$$

$$D(s)_{net} = G_{Tn}(s)(1 - Q_o(s)) + Q_o(s)G_T(s)\ .$$

If DLTC is used alone as compensator then in (41), $G_T(s)_{net} = G_T(s)$ and $G_{uc}(s)_{net} = G_{uc}(s)_{dltc}$. If SLTC-alone is used then $G_T(s)_{net} = G_T(s)$ and $G_{uc}(s)_{net} = G_{uc}(s)_{sltc}$. If DOB-alone is used then $G_T(s)_{net}$ is given by (42) and $G_{uc}(s)_{net} = G_{uc}(s)_{dob} = \frac{G_{Tn}(s)(1 - Q_o(s))G_B(s)}{D(s)_{net}}$.

5.2. Un-compensated gain of DOB-based-DLTC

For the system in (41), $G_{uc}(s)_{net}$ represents the net uncompensated gain left by DOB-based-DLTC due to modelling uncertainties and imperfect filtering. Under ideal filtering assumption for the frequencies with in the bandwidth, where $Q_o(s) \approx 1$, it follows from (41) that $G_{uc}(s)_{net} \approx 0$ which leads to the output of the net compensated system to be

$$w_o \approx \frac{1}{\eta} G_T(s)_{net}\ \tau_a^* \ \approx \frac{1}{\eta}\ G_{Tn}(s)\ \tau_a^*\ . \tag{42}$$

Therefore, for frequencies with in the bandwidth of $Q_o(s)$, the net compensated system in behaves like a nominal system with no load toque disturbance. Similarly, under ideal filtering assumptions for frequencies greater than the bandwidth of $Q_o(s)$ where $Q_o(s) \approx 0$, it follows from (41) that the output of the net compensated system is given as

$$w_o \approx \ \frac{1}{\eta} G_T(s)\ \tau_a^* + \frac{1}{\eta^2} G_{uc}(s)_{dltc}\ \tau_{Lo}\ . \tag{43}$$

Therefore, for higher frequencies where $Q_o(s) \approx 0$, $G_{uc}(s)_{net}$ approaches $G_{uc}(s)_{dltc}$. Since $|G_{uc}(s)_{dltc}|$ is always significantly less than that of $|G_B(s)|$, the use of DLTC in conjunction with DOB significantly reduces the net uncompensated gain $G_{uc}(s)_{net}$ for the load-torque. $|G_{uc}(s)_{net}|$ for the DOB-based-DLTC is plotted vs frequency in Fig. 12 in comparison with the $|G_{uc}(s)_{dltc}|$,$|G_{uc}(s)_{sltc}|$ and $|G_{uc}(s)_{dob}|$. To consider the worst-case scenario for the additive parametric uncertainty limited by p_{max}, the drive dominant actual-parameters are perturbed as per (28) while the non-dominant actual-parameters listed in Tables 1–3 are randomly perturbed at the most by p_{max}. It is seen from Fig. 12 that the

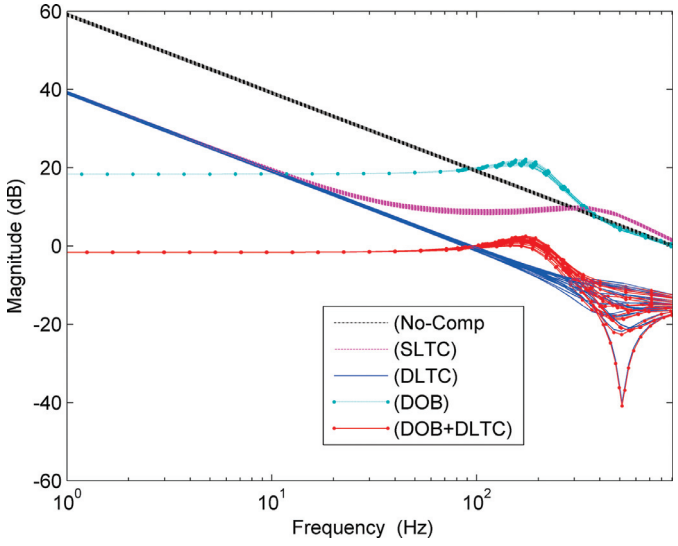

Fig. 12. Shows the magnitude plot of the net un-compensated gain $|G_{uc}(s)_{net}|$ vs frequency for the proposed DOB-based-DLTC in comparison with un-compensated magnitude gains $|G_{uc}(s)_{dltc}|$, $|G_{uc}(s)_{sltc}|$,$|G_{uc}(s)_{dob}|$ and no compensator, with the maximum uncertainty in actual motor parameters of the drive limited by p_{max}, for the motor parameters listed in Tables 1–3.

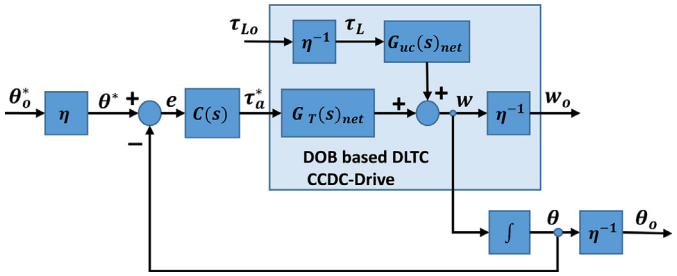

Fig. 13. A joint-level position feedback control of CCDC-drive with DOB-based-DLTC.

$|G_{uc}(s)_{net}|$ for the DOB-based-DLTC is constant for load-torque frequencies till 100 Hz, and hence in contrast to SLTC-alone and DLTC-alone gives a uniform improved compensation performance for all practical load-torque frequencies. The reduction in $|G_{uc}(s)_{net}|$ in comparison with $|G_{uc}(s)_{sltc}|$ is seen to be more than 25-dB for the load-torque at low frequencies (less than 5 Hz). This significant reduction in the un-compensated gain for the DOB-based-DLTC is expected to cause a significant improvement in compensating the load-torque disturbance τ_{Lo} in the low frequency range with low gear ratios.

6. Joint level servo control of CCDC-drive with DOB-based-DLTC

Depending on the task space control requirement, respective desired trajectories need to be tracked in the joint space of the exoskeleton [9]. The task space tracking performance is hence dependent on how well these desired joint trajectories are tracked in the presence of joint load-torque disturbance. The compensated CCDC-drive system in (41), under position servo control is shown in Fig. 13. The closed-loop position tracking performance of the compensated servo system is analysed for a standard PD-controller. It is seen from (42) that under ideal conditions, the actual forward system $G_T(s)_{net}$ behaves like a nominal system $G_{Tn}(s)$. The nominal feedforward transfer function in Fig. 13 is therefore given as $G_{fn}(s) = \frac{G_{Tn}(s)}{s}$. Using this $G_{fn}(s)$, a PD controller $C(s)$ with first order differential filter is designed for desired closed-loop bandwidth. $C(s)$ is therefore given by

$$C(s) = \frac{K_d(\tau_1 s + 1)}{(\tau_2 s + 1)}\ . \tag{44}$$

Under no measurement noise assumption, the output-angular position θ_o for the closed-loop system in Fig. 13, can therefore be given from (41) and (44), in terms of sensitivity $S(s)$ and complementary sensitivity $T(s)$, for a reference output-angular position θ_o^* as [20]

$$\theta_o = T(s)\theta_o^* + \frac{1}{\eta^2} S(s) G_{uc}(s)_{net}\tau_{Lo}, \tag{45}$$

where $L(s) = C(s)\frac{G_T(s)_{net}}{s}$,

$$S(s) = (1 + L(s))^{-1},$$

$$T(s) = L(s)(1 + L(s))^{-1}.$$

If the position-error e_θ is defined as $e_\theta = \theta^* - \theta$, where θ^* represents the desired positon of motor-shaft, then e_θ can be written from (45) as

$$e_\theta = S(s)\theta^* - \frac{1}{\eta} S(s) G_{uc}(s)_{net}\tau_{Lo}\ . \tag{46}$$

It is seen from (46) that increasing the loop gain $L(s)$ (by increasing the controller gain), decreases the sensitivity $S(s)$ which in turn decreases the effect of uncompensated gain $G_{uc}(s)_{net}$ for the disturbance input τ_{Lo}. This results in a reduced tracking error of the closed-loop system in Fig. 13. This reduction in tracking error comes at the cost of increased control effort τ_a^* and a decreased robustness of the closed-loop system [20].

A large τ_a^* dictates a large τ_e^* and hence a large reference armature

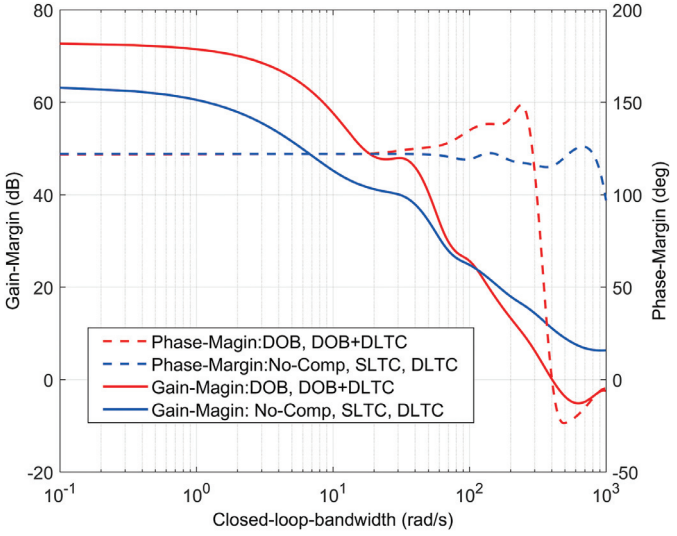

Fig. 14. Gain-margins and phase-margin of the system in Fig. 13 for different compensators, plotted for increasing closed-loop bandwidth.

current i_{as}^*. Since the CCDC-drive is a physical system, the value of i_{as}^* corresponding to τ_e^* is bounded by $I_{s\max}$. Furthermore, the gain and phase margin for the system in Fig. 13 are plotted in Fig. 14 for increasing closed-loop-bandwidth, for different compensators. It is seen from Fig. 14 that both the margins and hence in turn, the relative stability of the compensated servo system decreases with increasing closed-loop-bandwidth. Therefore, to ensure sufficient robustness for the system, the loop gain $L(s)$ and hence the closed-loop-bandwidth of the system is to be limited [22]. For the given drive parameters, the maximum closed-loop-bandwidth of the system is limited to 256 rad/s, which in turn gives a gain margin of 10 dB for the proposed compensator.

The maximum output-bandwidth for the system with the chosen gear ratio is therefore limited to 10 rad/s. (output-bandwidth = closed-loop-bandwidth / gear-ratio). With limited $L(s)$, it is clear from (45) and (46) that the only way to reduce the effect of the disturbing torque τ_{Lo} for a given gear ratio η, is by reducing the net un-compensated gain $G_{uc}(s)_{net}$. Therefore, compensators that can effectively reduce the gain $G_{uc}(s)_{net}$ would be able to practically improve the joint tacking performance in the presence of rated load-torque disturbance. The corresponding desired electromagnetic torque τ_e^*, to be generated by the CCDC-drive is then given form (35), (36) and (46) as

$$\tau_e^* = \frac{1}{(1 - Q_o(s))}\tau_a^* - \frac{Q_o(s)}{G_{Tn}(s)(1 - Q_o(s))}w \ . \tag{47}$$

The acceleration torque reference τ_a^* in (47) as control effort for the controller $C(s)$, is given from (46) as

$$\tau_a^* = \eta C(s)S(s)\theta_o^* - \frac{1}{\eta}C(s)S(s)G_{uc}(s)_{net}\tau_{Lo} \ . \tag{48}$$

The motor-shaft angular velocity w in (47) is given from (45) as derivative of the position θ_o, in terms of $S(s)$ and $T(s)$ as

$$w = \eta\frac{d\theta_o}{dt} = s\eta\theta_o = \eta sT(s)\theta_o^* + \frac{1}{\eta}sS(s)G_{uc}(s)_{net}\tau_{Lo}. \tag{49}$$

To effectively analyse the system in Fig. 13 for reference current requirements, a closed form expression for the armature current reference signal i_{as}^* (in volts) is found from (10),(11), (29),(48) and (49) in terms of the two inputs θ_o^* and τ_{Lo} as

$$i_{as}^* = \eta G_{i\theta}(s)\ \theta_o^* + \frac{1}{\eta}G_{i\tau_L}(s)\ \tau_{Lo}. \tag{50}$$

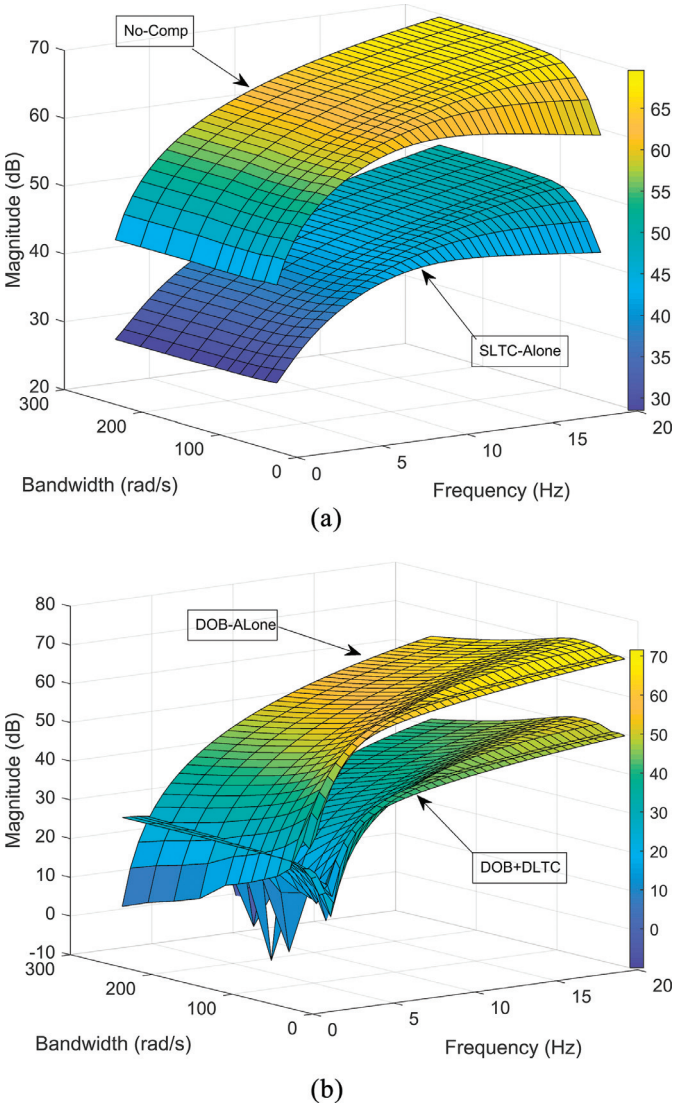

Fig. 15. Surface plot of $|G_{i\tau_L}(s)|$ for the system in Fig. 13, plotted vs load-torque frequency and closed-loop-bandwidth. a) For no compensator and SLTC-alone. b) For DOB-alone and DOB-based-DLTC.

where

$$G_{i\theta}(s) = \frac{H_c}{k_{tn}(1 - Q_o(s))}\left(C(s)S(s) - \frac{sT(s)Q_o(s)}{G_{Tn}(s)}\right),$$

$$G_{i\tau_L}(s) = N_{Dcf}(s) - \frac{sH_cG_{uc}(s)_{dltc}(C(s) + sQ_o(s))}{k_{tn}(sD(s)_{net} + C(s)G_T(s)\ G_{Tn}(s))}.$$

If DOB -Alone is used as compensator in (50), then $N_{Dcf}(s) = 0$ and $G_{uc}(s)_{dltc} = G_B(s)$. For DLTC or SLTC-alone, $Q_o(s) = 0$ with appropriate $G_{uc}(s)_{dltc}$ or $G_{uc}(s)_{sltc}$. Improvement offered by the proposed compensator w.r.t the armature current reference requirement is shown in Fig. 15. $|\ G_{i\tau_L}(s)|$ defined in (50) is plotted as a surface vs load-torque frequency and the allowed closed-loop-bandwidth for different compensators. It is seen that $|\ G_{i\tau_L}(s)|$ for the proposed DOB-based-DLTC is the least over nearly all the practical load-torque frequencies (< 10 Hz) and allowed closed-loop-bandwidths (< 256 rad/s) and hence is expected to require the least i_{as}^* as compared to DOB and SLTC-alone, in compensating the load-torque disturbances.

Table 4
Parameters for 4-DOF human-exoskeleton system in Fig. 1.

Type	Quantity	Symbol	Value
Human arm	Link Mass (Kg)	m_{1h}, m_{2h}, m_{3h}, m_{4h}	0, 0, 2.64, 1.93
Exoskeleton		m_{1e}, m_{2e}, m_{3e}, m_{4e}	1.73, 1.75, 1.76, 0.7
Exoskeleton	D-H parameters	d_1, a_1, α_i, θ_{o1}	0, -0.2, $\pi/2$, $\pi/2$
		d_2, a_2, α_2, θ_{o2}	0, 0, $-\pi/2$, $3\pi/2$
		d_3, a_3, α_3, θ_{o3}	0.33, 0.065, 0, 0
		d_4, a_4, α_4, θ_{o4}	0.25, -0.065, 0, $\pi/6$

7. Simulation results

7.1. Exoskeleton and CCDC-drive parameters

To obtain realistic simulation results, the proposed DOB-based-DLTC is simulated and compared for performance for a single joint, by using the practically real parameters of the CCDC-drive. Table 1 lists the independent parameters for the drive, along with their nominal values. The dependent parameters for the drive are found explicitly in terms of its independent parameters and are listed in Table 2. The parameters for the four-quadrant power converter are listed in Table 3. The parameters for the designed 4-DOF arm exoskeleton shown in Fig. 1 are given in the Table 4. The human arm limb parameters are found for an 88 Kg man with a height of 178 cm [46].

7.2. Joint level tracking performance comparison

For the closed-loop system in Fig. 13(a) position tracking response is simulated using the proposed DOB-based-DLTC, in comparison with SLTC-alone, DLTC-alone and DOB-alone is shown in Fig. 17. A low magnitude sinusoidal position trajectory at 1.6 Hz (10 rad/s) is given as a reference, to clearly see the improvement offered by the proposed compensator. A rated sinusoidal load-torque disturbance (shown in Fig. 16) is given as τ_{Lo}. The maximum uncertainty in the non-dominant actual motor parameters of the drive is still limited by p_{max}, while the dominant actual parameters are perturbed as per (28). A PD controller given by (44) is designed to give the maximum allowed closed-loop-bandwidth of 256 rad/s with a gain margin of 10 dB and a phase margin of 120°. The armature current reference signal i_{as}^* for different compensators is found using (50) and is plotted in Fig. 18. It is seen from Figs. 17 and 18 that the proposed DOB-based-DLTC in comparison with the other compensators, gives the least tracking error for the given reference trajectory, under rated load-torque disturbance, with the least i_{as}^* requirement. Thus, with the proposed compensator, the CCDC-drive based joint actuator shows significantly good servo control performance, without compromising the linearity of the system in Fig. 13.

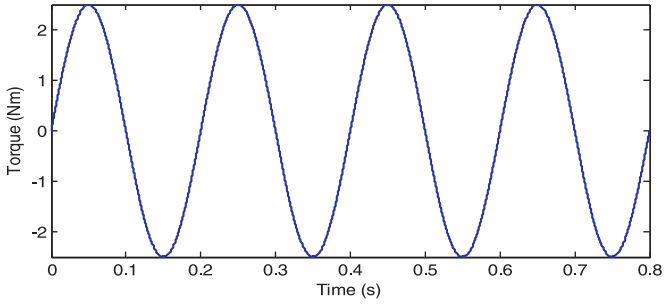

Fig. 16. 2.5 Nm joint load-torque disturbance τ_{Lo} at 5 Hz.

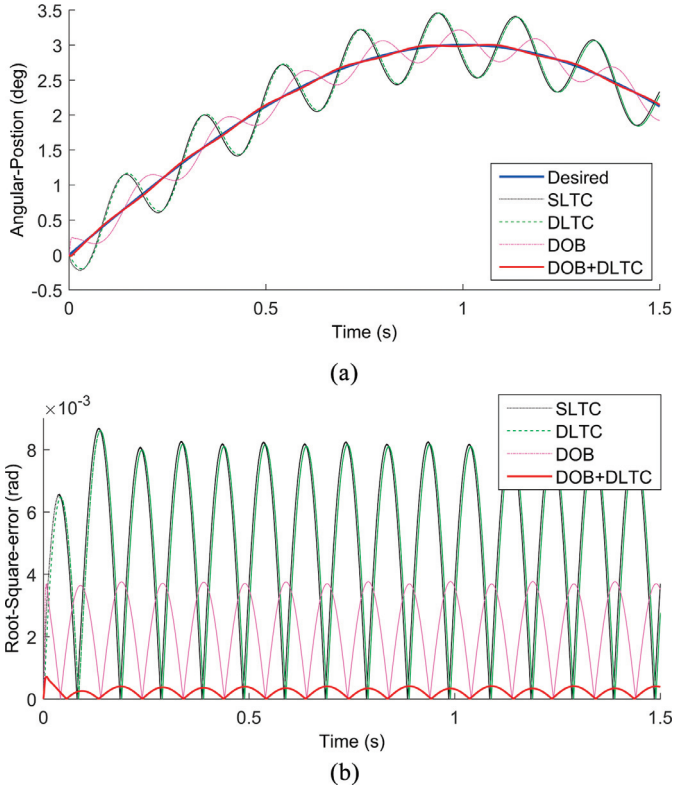

Fig. 17. a) Tracking response for DOB-based-DLTC scheme plotted in comparison for different compensators for system in Fig. 13 for a load-torque given by Fig. 14. Additive uncertainty in actual parameters is limited by p_{max}. (b): Root square tracking error for DOB-based-DLTC is plotted in comparison.

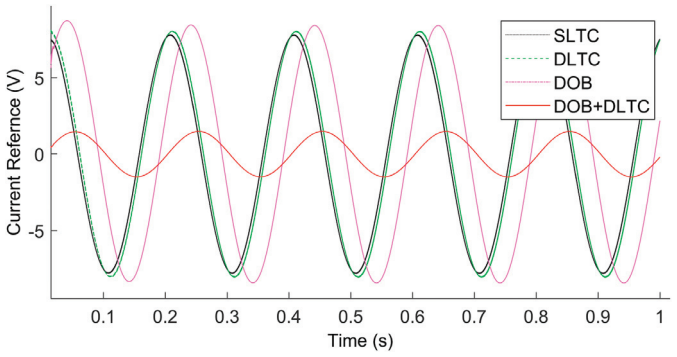

Fig. 18. Comparative plots of armature current reference i_{as}^* in volts for different compensators for the system in Fig. 13 with of closed-loop-bandwidth of 256 rad/s.

8. Experimental results

8.1. Experimental setup

To experimentally evaluate and compare the compensation performance of the proposed compensator scheme for a joint level CCDC-drive, an xPC-Target™ based torque test rig is designed to ensures both real-time performance and Matlab/Simulink™ compatibility. The designed experimental setup is shown in Fig. 19. A detailed closeup view of the load-torque test rig is shown in detail in Fig. 20. The torque test rig is composed of a variable load-torque generator, a load toque sensor with signal conditioning and a CCDC-drive under test. The xPC—Host computer hosts the Simulink™ section of the code for different compensators and is linked to the xPC-Target computer through a dedicated Ethernet link. xPC-Host computer not only generates and downloads

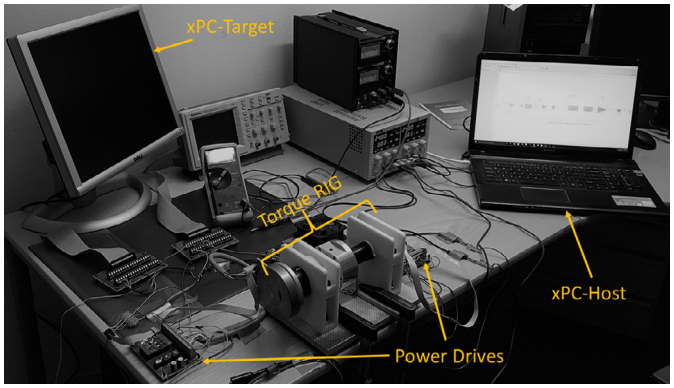

Fig. 19. Experimental setup for evaluating the torque compensation performance of a joint level CCDC-drive using the proposed compensator.

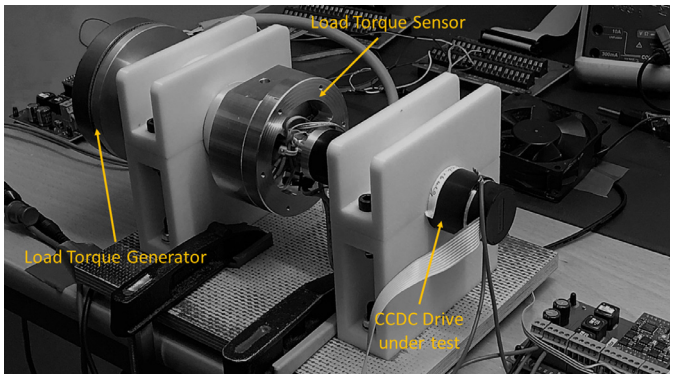

Fig. 20. Showing component level detail of load-torque testing rig.

the real-time code to the xPC-Target but also is used to control the x-PC target properties, display and datalogging in real time. xPC-Target computer on the other hand not only implements the code for different torque compensator schemes for the CCDC-drive in real time but also generates a rated sinusoidal load-torque at 1.6 Hz, by controlling a separate DC motor acting as load-torque generator. An xPC-Target™ supported multifunction I/O card by Humusoft™ is used to provide the necessary hardware interface for CCDC-drive, load-torque generator and torque sensor.

8.2. Experimental results

The CCDC-drive (whose parameters are listed in Tables 1–3) is first held at a constant fixed angular position while a variable load-torque is applied by the load-torque generator at the output shaft of the CCDC-drive.

An indigenously designed torque sensor and conditioning card are used in conjunction to sense the respective generated load torques for the different compensation schemes. These load-torques and are shown in Fig. 21 and are seen to be comparable in magnitude and frequency. The compensation improvement afforded by the different load-torque compensators is then measured as deviation of the angular position from the nominal shaft position. This deviation under respective rated load torques is shown in Fig. 22. The performance of the proposed compensator is also compared and verified experimentally for position tracking, under respective experimental load torques of Fig. 24. A low magnitude sinusoidal trajectory at 0.25 Hz is given as desired trajectory to clearly see the improvement afforded by the proposed compensator. The tracking results are shown in Fig. 24. It is seen that the CCDC-drive tracks the desired trajectory very closely for the proposed compensator. The corresponding practical instantaneous improvement in compensating the load-torque offered by the proposed compensator w.r.t to

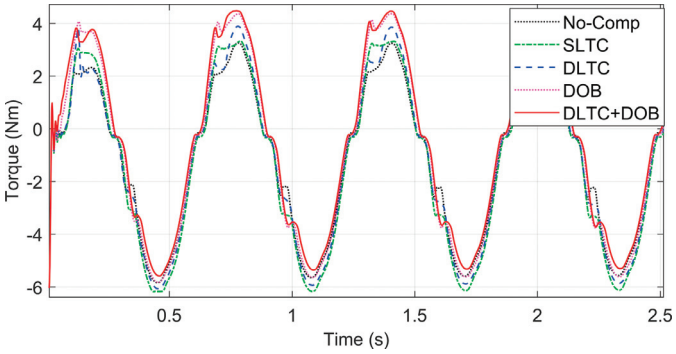

Fig. 21. Experimental load-torque applied by the load-torque generator at the output shaft of CCDC-drive for different compensator schemes.

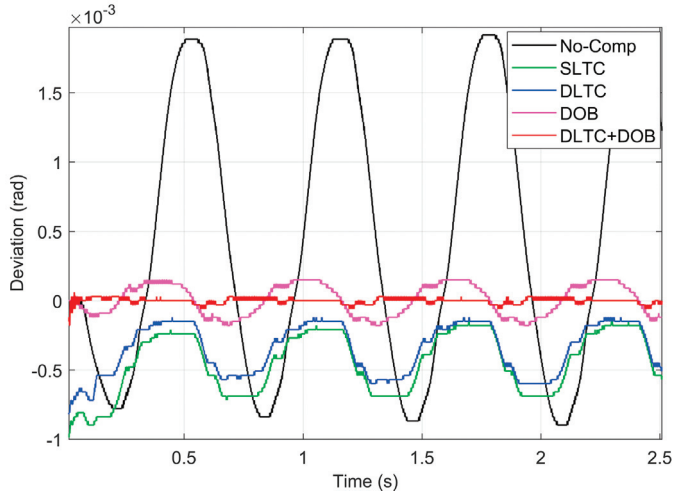

Fig. 22. Experimental results for CCDC-drive output shaft deviation from the nominal position, for different load-torque compensators, under respective experimental load-torques of Fig. 21.

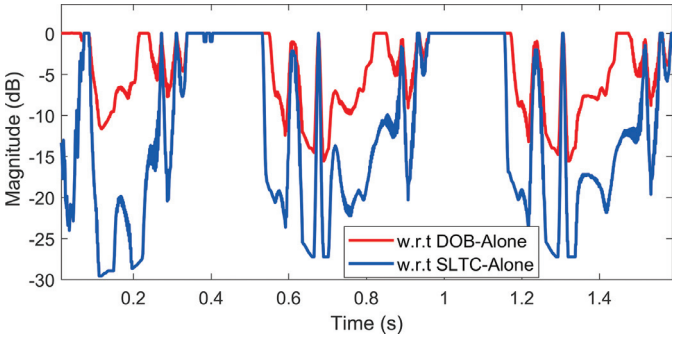

Fig. 23. Practical instantaneous improvement offered by the proposed DOB-DLTC in compensating the load torques as compared to DOB-alone and SLTC-alone for experimental results shown in Fig. 22.

DOB-alone and SLTC-alone is shown in Fig. 23. This in turn gives a mean improvement in compensation of 5-dB w.r.t DOB-alone and 12-dB w.r.t SLTC -Alone.

The proposed DOB-based-DLTC hence practically shows to give a significantly improved load-torque compensation performance. Therefore, if the proposed compensator scheme is applied to all the n active joints of the exoskeleton, it can more effectively compensate for the uncertain-nonlinear coupling vector $\boldsymbol{f}_n$ in (5) as compared to SLTC and DOB-alone. Mean 5-dB improved load-torque compensation performance w.r.t DOB-alone per joint is significant, as each active joint of the exoskeleton would be able to suppress the respective load- torque

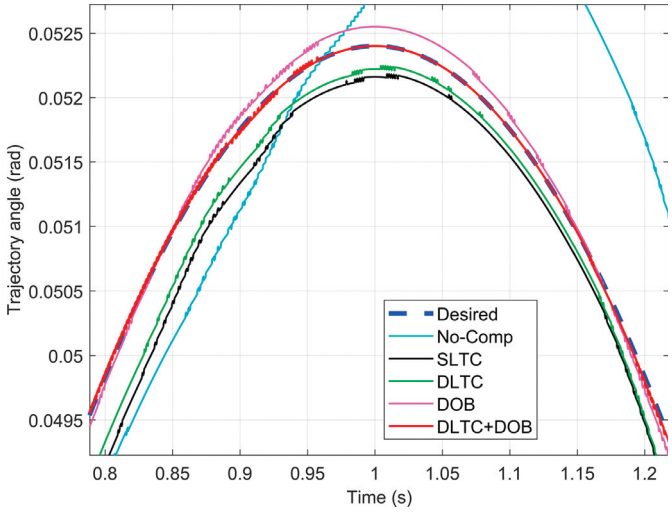

Fig. 24. Experimental tracking results of CCDC-drive for different load-torque compensators, under respective experimental load torques of Fig. 21.

disturbance 1.8 times more effectively and four times more effectively as compared to SLTC-alone. This in turn means that the uncompensated uncertain-nonlinear vector term $\boldsymbol{e}_{uc}$ in (7) is significantly smaller. Therefore, the human-exoskeleton system in (7) is more effectively linearized and decoupled with the proposed DOB-based-DLTC, in presence of uncertain-nonlinear joint load toques, due to misalignment between human and exoskeleton axis of rotation and uncertainty in human /exoskeleton kinematics and dynamics. This hence in turn, allows linear joint controllers to be independently designed and achieve superior tracking performance, which in turn would significantly improve the task space tracking performance of the human-exoskeleton system. The inclusion of the higher order dynamics in DLTC comes at the cost of having shorter sampling time t_s ($t_s < 30$ μs from Fig. 4). But with modern processors, implementation of the proposed compensator at shorter sampling time is easily possible.

9. Conclusion

In this paper, it is shown that in exoskeleton applications the uncertain human dynamics appears as uncertain load-torques for the actuators of the exoskeleton, which cannot be ignored for low gear ratio actuators. A DOB-based-DLTC in a feedback-feedforward structure, is therefore proposed and analysed for compensation performance, for the joint level servo control of CCDC-drive actuators of the exoskeleton with small gear ratios. It is shown both theoretically and practically that the proposed compensator gives at least a 5-dB mean improved performance w.r.t DOB-alone, and a 12-dB mean improvement w.r.t SLTC-alone for rated load-torque frequencies up to 1.6 Hz with 10% drive-parametric uncertainty. The proposed compensator is further analysed and shown to give comparable reference current requirements for the compensated CCDC-drive under joint level servo control. The improved compensation performance of the proposed DOB-based-DLTC compensator for CCDC-drive is experimentally verified by using xPC-Target™ based load-torque rig. In the presence of uncertain load-torques due to the human-exoskeleton interactions, it is strongly expected that the improvement offered by the proposed DOB-based-DLTC in compensating the joint level uncertain load torques would in turn significantly improve the task space performance of the exoskeleton as well.

Acknowledgment

This work was supported in part by the Ambient Assistance Living (AAL) Program under Grant AAL-2013-6-042.

A. Appendix

A.1. Accurate frequency domain model of CCDC-drive

For the CCDC-drive shown in Fig. 2 the dynamics of all the subcomponents are considered to find an accurate model of the CCDC-drive in frequency domain. The model is derived for motor-shaft angular velocity 'w' in terms of armature current reference i_{as}^{*} and load-torque τ_L for the drive parameters listed in Tables 1–3. The effect of the gearhead is considered on the model separately.

A.1.1. PWM power converter

In Fig. 2 with v_c as an input control voltage and V_a as the average DC output voltage, the PWM converter is modelled as a first order system $G_r(s)$ as [45].

$$G_r(s) = \frac{V_a(s)}{v_c(s)} = \frac{K_r}{(0.5\ t_r s + 1)}, \quad \text{where } K_r = \frac{V_{dc}}{v_{c_{\max}}}. \tag{A.1}$$

A.1.2. Armature-current dynamics

For a CCDC-drive armature current i_a of the motor is controlled in feedback. Therefore, i_a in terms of V_a and τ_L is given as

$$i_a = G_a(s).\ V_a + \ G_\tau(s).\ \tau_L, \tag{A.2}$$

$$\text{where} \quad G_a(s) = \frac{(1+\tau_n s)k_a}{D(s)}, \ G_\tau(s) = \frac{k_a k_b\ K_n}{D(s)},$$
$$D(s) = (1 + \tau_a s)(1 + \tau_n s) + k_a k_b k_t\ K_n.$$

A.1.3. Current controller

If actual armature current i_a is bounded to $I_{a_{max}}$ amperes and the sensed armature current i_{as} is bounded to $I_{s_{\max}}$ in volts. Then the current sensor gain H_c is defined as $H_c = I_{s_{\max}}/I_{a_{max}}$. To ensure a small steady state error in i_a a PI controller $G_c(s)$ is selected as the current controller as

$$G_c(s) = K_c/s \tag{A.3}$$

A.1.4. Mechanical dynamics

Referring to Fig. 2 the motor angular velocity w in terms of the mechanical dynamics of the motor is given by

$$w = G_m(s)(\tau_e - \tau_L) = \frac{K_m}{(1+\tau_m)}(k_t i_a - \tau_L), \tag{A.4}$$

which can then be written in terms of two inputs i_a and τ_L as

$$w = \frac{K_m k_t}{(1+\tau_m)} i_a - \frac{K_m}{(1+\tau_m)}\tau_L\,. \tag{A.5}$$

From (A.2)–(A.5), w can then be written in terms of V_a and τ_L as

$$w = G_1(s).\ V_a + G_2(s).\ \tau_L\,, \tag{A.6}$$

where $G_1(s) = \frac{k_a k_t K_n}{D(s)}$, $G_2(s) = \frac{K_n}{(1+\tau_n s)(1 - k_t G_\tau(s))}$.

A.1.5. Full closed-loop dynamics

From Fig. 2 V_a can also be written in terms of i_{as}^* and i_{as} as

$$V_a = G_c(s)G_r(s)(i_{as}^* - i_{as}). \tag{A.7}$$

Since $i_{as} = H_c\ i_a$, V_a in (A.7) is then given by

$$V_a = G_c(s)G_r(s)(i_{as}^* - H_c\ i_a)\,. \tag{A.8}$$

From (A.5)–(A.8), V_a can be written in terms of i_{as}^* and τ_L as

$$V_a = \frac{G_c(s)G_r(s)}{(1 + H_c G_c(s)G_r(s)G_a(s))} i_{as}^* - \frac{H_c\ G_c(s)G_\tau(s)G_r(s)}{(1 + H_c G_c(s)G_r(s)G_a(s))}\tau_L. \tag{A.9}$$

From (A.6) and (A.9) and by considering the zero-order hold effect in i_{as}^*, velocity w is found in terms of the inputs i_{as}^* and τ_L as

$$w = G_A(s).\ i_{as}^* - G_B(s).\ \tau_L, \tag{A.10}$$

where $G_A(s) = \frac{G_c(s)G_r(s)G_{zoh}(s)}{D_f(s)}$, $G_B(s) = G_D(s) + G_2(s)$,

$$G_D(s) = \frac{H_c G_c(s)\ G_\tau(s)G_r(s)}{D_f(s)}, \quad D_f(s) = (1 + H_c G_c(s)G_r(s)G_a(s)),$$

$$G_{zoh}(s) = \frac{1}{(1 + 0.5\ t_s\ s)},$$

Eq. (A.10) hence gives an accurate, higher order frequency domain model of the CCDC-drive.

A.1.6. Effect of gear head

If η is gear ratio of drive and τ_{Lo} is torque at the output shaft, then output angular velocity of the drive w_o is given from (A.10) in terms of i_{as}^* and τ_{Lo} as

$$w_o = \frac{1}{\eta}\ G_A(s).\ i_{as}^* - \frac{1}{\eta^2} G_B(s).\ \tau_{Lo}\ . \tag{A.11}$$

It is seen from (A.11) that for smaller gear ratios $1/\eta^2$ is not a small quantity therefore to reduce the effect of τ_{Lo} on w_o the gain $G_B(s)$ must be small over the effective bandwidth of the drive.

A.2. Approximate frequency domain model of CCDC-drive

A first order approximate model for the CCDC-drive can be obtained from (A.10) if it is assumed that $\tau_a \ll \tau_n$. This in turn implies that $D(s)$ in (A.2) can then be written approximately as

$$D'(s) = a\left(1 + \frac{\tau_n}{a}s\right) \text{ where } a = 1 + k_a\ k_b\ k_t\ K_n\ . \tag{A.12}$$

From (A.12) while assuming $t_r \ll 1$ and $\frac{\tau_n}{a} \ll 1$, $G_A(s)$ in (A.10) can be written as a first order approximation as

$$G_A'(s) = \frac{K_A}{(1 + \tau_A s)}, \tag{A.13}$$

where $K_A = \frac{k_t\ K_n}{H_c}$, $\tau_A = \frac{a + H_c K_c \tau_n k_a K_r}{H_c K_c \tau_n k_a K_r}$.

Similarly, from the above assumptions transfer functions in (A.1), (A.2) and ((A.6) can then be written approximately as

$$G_r'(s) = K_r, \quad G_a'(s) = \frac{k_a(1+\tau_n s)}{a}, \quad G_\tau'(s) = \frac{k_a k_b\ K_n}{a}, \quad G_1'(s) = \frac{k_a k_t\ K_n}{a}, \quad G_2'(s) = \frac{K_n}{a}. \tag{A.14}$$

From (A.14), $G_D(s)$ defined in (A.10) is then approximated as

$$G'_D(s) = \frac{K_D}{(1+\tau_D)} \text{ where } K_D = \frac{K_n(a-1)}{a}, \ \tau_D = \tau_A \ . \tag{A.15}$$

From (A.14) and (A.15), $G_{B_n}(s)$ in (A.10) can be approximated as

$$G'_B(s) = \frac{K_B}{(1+\tau_B s)} \text{ where } K_B = K_n, \ \tau_B = \tau_D = \tau_A. \tag{A.16}$$

Therefore, a first order approximate model of the CCDC-drive can be written from (A.10), (A.15) and (A.16) as

$$w = G'_A(s).\ i^*_{as} - G'_B(s).\ \tau_L. \tag{A.17}$$

With gear head included the approximate CCDC-drive model in (A.17) is given as

$$w_o = \frac{1}{\eta}G'_A(s).\ i^*_{as} - \frac{1}{\eta^2}G'_B(s).\ \tau_{Lo}. \tag{A.18}$$

References

[1] Ansari A, Atkeson CG, Choset H, Travers M. A survey of current exoskeletons and their control architectures and algorithms. Carnegie Mellon University; 2015. Oct.
[2] Gopura RARC, Kiguchi K, Bandara DSV. A brief review on upper extremity robotic exoskeleton systems. 6th inter. conf. on industrial and information systems. 2011.
[3] Hogan N. On the stability of manipulators performing contact tasks. IEEE Trans Robot Autom 1998;4(December (6)):667–86.
[4] Colgate JE, Hogan N. Robust control of dynamically interacting systems. Int J Control 1988;48:65–88.
[5] Artemiadis PK, Katsiaris PT, Liarokapis MV, Kyriakopoulos KJ. Human arm impedance: characterization and modeling in 3D space. The 2010 IEEE Int. conf. on intelligent robots and systems, Taipei, Taiwan, October 18-22. 2010.
[6] Rosen J, Perry JC, Manning N, Burns S, Hannaford B. The human arm kinematics and dynamics during daily Activities –toward a 7 DOF upper limb powered exoskeleton. 12th int. conf. on advanced robotics, July. 2005. p. 18–20.
[7] Tee KP, Burdet E, Chew CM, Milner TE. A model of force and impedance in human arm movements. Biol Cybern 2004;95(5):368–75. May.
[8] Pons JL. Wearable robots: biomechatronic exoskeletons. John Wiley & Sons; 2008.
[9] Lewis FL, Dawson DM, Abdallah CT. Robot manipulator control theory and practice. 2nd Ed. New York: Marcel Dekker; 2004.
[10] Paul RP. Robot manipulators. Cambridge: MIT Press; 1981.
[11] Shaari N, Md Isa I, Jun T. Torque analysis of lower limb exoskelton robot design. ARPN J Eng Appl Sci 2015;10(October (19)):9141–9.
[12] Redlarski G, Blecharz K, Dąbkowski M, Pałkowski A. Comparative analysis of exoskeletal actuators. Pomiary Automatyka Robotyka 2012;16:133–8.
[13] Hollerbach IW. A comparative analysis of actuator technologies for robotics. Robotic review 2. Cambridge, MA, USA: MIT Press; 1991.
[14] Önen Ö, Botsalı FM, Kalyoncu M, Tınkır M, Yılmaz N, Sahin Y. Design and actuator selection of a lower extremity exoskeleton. IEEE Trans Mechtron 2014;19(2):623–31.
[15] Vallery H, Veneman J, Asseldonk EV, Ekkelenkamp R, Buss M, Der Kooij HV. Compliant actuation of rehabilitation robots. IEEE Rob Autom Mag 2008;15(September (3)):60–9.
[16] Tagliamonte LN. pHrI in assistive and rehabilitaiton robots Joints and actuator design. Rome: Dept. Bio Medical Eng., Università Campus Bio-Medico; 2012.
[17] Nakamura Y, Hanafusa H. Optimal redundancy control of robot manipulators. Int J Rob Res 1987;6(1):32–42.
[18] Hsu P, Hauser J, Sastry. Dynamic control of redundant manipulators. J Rob Syst 1989;6(2):133–48.
[19] Nakanishi J, Cory R, Mistry M, Peters J, Schaal S. Operational space control: a theoretical and empirical comparison. Int J Rob Res 2008;27(June (6)):737–57.
[20] Skogestad S, Postlethwaite I. Multivariable feedback control analysis and design. John Wiley & Sons; 2005. Aug.
[21] Goldfarb M, Sirithanapipat T. The effect of actuator saturation on the performance of PD-controlled servo systems. Mechatronics 1999;9:497–511.
[22] Saberi A, Stoorvogel A. Special issue on control problems with constraints. Int J Robust Nonlinear Control 1999;9(10):583–734.
[23] Dixon WE. Adaptive regulation of amplitude limited robot manipulators with uncertain kinematics and dynamics. IEEE Trans Autom Control 2007;52(3):448–93.
[24] Su YX, Müller PC, Zheng CH. Global asymptotic saturated PID control for robot manipulators. IEEE Trans Control Syst Technol 2010;18(November (6)):1280–8.
[25] Buja GS, Menis R, Valla MI. Disturbance torque estimation in a sensorless DC drive. IEEE Trans Indus Electron 1995;42(August (4)):351–7.
[26] Grignion D, Chen X, Kar N, Qian H. Estimation of load disturbance torque for DC motor drive systems under robustness and sensitivity consideration. IEEE Trans Indus Electron 2014;61(February (2)):930–42.
[27] Grignion D. Robust load disturbance torque estimation for a permanent magnet DC motor drive system MSc Thesis Dept. of Electrical and Computer Eng., University of Windsor; 2012.
[28] Srisertpol J, Khajorntraidet C. Estimation of DC motor variable torque using adaptive compensation. 2009 chinese control and decision conference. 2009.
[29] Lee SC, Ahn HS. Sensorless torque estimation using adaptive kalman filter and disturbance estimator. *Proc. of 2010 IEEE/ASME Int. Conf. On Mechatronic and Embedded Systems and Applications*, Qingdao, ShanDong, 2010. 2010. p. 87–92.
[30] Ohnishi K. A new servo method in mechatronics. Trans Jpn Soc Electr Eng 1987;107-D:83–6. Vols.
[31] Endo S, Kobayashi H, Kempf CJ, Kobayashi S, Tomizuka M, Hori Y. Robust digital tracking controller design for high-speed positioning systems. Control Eng Practice 1996;4(4):527–36.
[32] Fujiyama K, Tomizuka M, Katayama R. Digital tracking controller design for CD player using disturbance observer,"of the pp. 598–603, 1998. Proc. int. workshop on advanced motion control. 1998.
[33] Lee HS, ". Tomizuka M. Robust motion controller design for high-accuracy positioning systems. IEEE Trans Indus Electron 1996;43(1):48–55.
[34] Ryooa JR, Doh T-Y, Chung MJ. Robust disturbance observer for the track-following control system of an optical diskdrive. Control Eng Pract 2004;12:587. -585.
[35] Hori Y. High performance control of robot manipulator without using inverse dynamics. Control Eng Practice 1993;1(3):529–38.
[36] Kong K, Bae J, Tomizuka M. Control of rotary series elastic actuator for ideal force-mode actuation in human-robot interaction applications vol. 14, no. 1, pp. 1–14, 2009 IEEE/ASME Trans Mechatron 2009;14(1):1–14.
[37] Kong K, Moon H, Hwang B, Jeon D, Tomizuka M. "Impedance compensation of SUBAR for back-drivable force mode actuation. IEEE Trans Rob 2009;25(3):512–21.
[38] Dean JC, Kuo AD, Alexander NB. Age-related changes in maximal hip strength and movement speed. J Gerontol 2004;vol. Vol. 59A(3):286–92.
[39] Gross M, Stevenson PJ, Charette SL, Pyka G, Marcus R. Effect of muscle strength and movement speed on the biomechanics of rising from a chair in healthy elderly and young women. ELSEVIER:Gait Posture 1998;8:175–85.
[40] Schearer EM. Identifying inverse human arm dynamics using a robotic testbed. IEEE/RSJ int. conf. on intelligent robots and systems, Chicago, IL, 2014. 2014. p. 3585–91.
[41] Dolan JM, Friedman MB, Nagurka ML. Dynamic and loaded impedance components in the maintenance of human arm posture. IEEE Trans Syst Man Cybern 1993;23(9):698–709. May/Jun.
[42] Taniguchi S. Inverse dynamics of human passivemotion based on Iterative learning control. IEEE Trans Syst Man Cybern - Part A 2012;42(March (2)):307–15.
[43] Popoola JJ, Oladejo Charity OJ, Odeyemi S. Modelling and simulation of armature-controlled direct current motor using matlab. SSRG Int J Electr Electron Eng 2015;2(March (3)):19–25.
[44] Guedri B, Chaari A. Design of single closed loop control for chopper fed DC motor drive using IMC principles. 16th int. conf. on sciences and techniques of automatic control and computer eng. (STA). 2015. p. 493.
[45] Krishnan R. Electric motor drives: modeling analysis and control. New Jersey: Prentice Hall; 2001.
[46] "Man-System Integration Standards, Anthropometry and Biomechanics," National Aeronautics and Space Administration, [Online]. Available: http://msis.jsc.nasa.gov/sections/section03.htm.

Nauman Masud is currently working at Department of Electronics, Mathematics, and Natural Sciences, University of Gävle and he is a registered PhD student at Robotics, Perception, and Learning Laboratory at The Royal Institute of Technology in Stockholm (KTH). He received his B.Sc. Electrical Engineering degree of University of Engineering and Technology Peshawar, Pakistan. He received his M.Sc. System Engineering from Quaid-e-Azam University Islamabad, Pakistan. His current research interests include modeling and control of assistive exoskeletons, human-robot interaction and real time control of electromechanical systems.

Christian Smith is an Assistant Professor in Computer Science at the Robotics, Perception, and Learning Laboratory at The Royal Institute of Technology in Stockholm (KTH). He received his M.Sc. in Engineering Physics in 2005, and Ph.D. in Computer Science in 2009, both at KTH. He has been a post-doctoral researcher at Advanced Telecommunications Research International (ATR) in Kyoto, Japan. He is the secretary of the IEEE Robotics and Automation Society Swedish Chapter. Research interests include control and modelling for manipulation and grasping in human-centric environments and human–robot interaction.

Magnus Isaksson is a Professor, Department Head and the Head of Research at Department of Electronics, Mathematics, and Natural Sciences, University of Gävle. He received his M.Sc. degree in microwave engineering from the University of Gävle, Sweden, in 2000. The Licentiate degree from Uppsala University, Uppsala, Sweden, in 2006, and the Ph.D. degree from the KTH Royal Institute of Technology, Stockholm, Sweden, in 2007. In 2012, he was a Docent with the KTH Royal Institute of Technology. His current research interests include compensation of nonlinear modelling and characterization of devices and systems, signal processing, and assistive exoskeletons.